

## Enhancement of spin-charge conversion efficiency for $\text{Co}_3\text{Sn}_2\text{S}_2$ across transition from paramagnetic to ferromagnetic phase

Takeshi Seki <sup>1,\*</sup> Yong-Chang Lau <sup>1,2</sup> Junya Ikeda,<sup>1</sup> Kohei Fujiwara <sup>1</sup> Akihiro Ozawa <sup>1</sup> Satoshi Iihama <sup>3,4</sup>  
Kentaro Nomura,<sup>1,5</sup> and Atsushi Tsukazaki<sup>1,6</sup>

<sup>1</sup>*Institute for Materials Research, Tohoku University, Sendai 980–8577, Japan*

<sup>2</sup>*Institute of Physics, Chinese Academy of Sciences, Beijing 100190, China*

<sup>3</sup>*Frontier Research Institute for Interdisciplinary Sciences, Tohoku University, Sendai 980–8578, Japan*

<sup>4</sup>*WPI Advanced Institute for Materials Research, Tohoku University, Sendai 980–8577, Japan*

<sup>5</sup>*Department of Physics, Kyushu University, Fukuoka 819-0395, Japan*

<sup>6</sup>*Center for Science and Innovation in Spintronics, Core Research Cluster, Tohoku University, Sendai 980–8577, Japan*



(Received 31 July 2022; accepted 21 February 2023; published 31 March 2023)

$\text{Co}_3\text{Sn}_2\text{S}_2$  (CSS) is one of the shandite compounds and becomes a magnetic Weyl semimetal candidate below the ferromagnetic phase transition temperature ( $T_C$ ). In this paper, we investigate the temperature ( $T$ ) dependence of conversion between charge current and spin current for the CSS thin film by measuring the spin-torque ferromagnetic resonance (ST-FMR) for the trilayer consisting of CSS/Cu/CoFeB. Above  $T_C \sim 170$  K, the CSS/Cu/CoFeB trilayer exhibits the clear ST-FMR signal coming from the spin Hall effect in the paramagnetic CSS and the anisotropic magnetoresistance (AMR) of CoFeB. Below  $T_C$ , on the other hand, it is found that the ST-FMR signal involves the dc voltages ( $V_{dc}$ ) not only through the AMR but also through the giant magnetoresistance (GMR). Thus, the resistance changes coming from both AMR and GMR should be taken into account to correctly understand the characteristic field angular dependence of  $V_{dc}$ . The spin Hall torque generated from the ferromagnetic CSS, which possesses the same symmetry as that for spin Hall effect, dominantly acts on the magnetization of CoFeB. A definite increase in the spin-charge conversion efficiency is observed at  $T < T_C$ , indicating that the phase transition to the ferromagnetic CSS promotes the highly efficient spin-charge conversion. In addition, our theoretical calculation shows the increase in spin Hall conductivity with the emergence of magnetic moment at  $T < T_C$ , which is consistent with the experimental observation.

DOI: [10.1103/PhysRevResearch.5.013222](https://doi.org/10.1103/PhysRevResearch.5.013222)

### I. INTRODUCTION

Creation, manipulation, and detection of the spin angular momentum flow, called spin current ( $\mathbf{J}_s$ ), are vital to an efficient operation of the spintronic devices. High efficiency in the conversion process between charge current ( $\mathbf{J}_c$ ) and  $\mathbf{J}_s$  is required for improving the device performance, reducing the power consumption, and leading to multifunctionalities. One of the promising ways for spin-charge conversion is to exploit the spin Hall effect (SHE) [1,2], which is mostly studied in nonmagnets (NMs). The conversion from  $\mathbf{J}_c$  to  $\mathbf{J}_s$  via SHE is expressed as

$$\mathbf{j}_s = \left( \frac{\hbar}{2e} \right) \alpha_{\text{SH}} (\mathbf{s} \times \mathbf{j}_c), \quad (1)$$

where  $\mathbf{j}_c$  and  $\mathbf{j}_s$  are charge-current density and spin-current density, respectively,  $\alpha_{\text{SH}}$  is the spin Hall angle,  $e (< 0)$  is

the electric charge of an electron,  $\hbar$  is the reduced Planck constant, and  $\mathbf{s}$  is the quantization axis of electron spin.  $\alpha_{\text{SH}}$  is a key parameter related to the spin-orbit coupling and the efficiency of spin-charge conversion. Thus, many studies were devoted to the development of spin Hall material with large  $\alpha_{\text{SH}}$ . It has been demonstrated that not only a NM but also a ferromagnet (FM) is utilized for the spin-charge conversion [3–27]. In the early stage, the conversion from  $J_s$  to  $J_c$  in FM was reported [3–5]. Then, it was predicted that the anomalous Hall effect (AHE) also generates  $J_s$ , which is called spin anomalous Hall effect (SAHE) [6], and the SAHE was examined for several FMs experimentally and theoretically [12,17,24,27]. Apart from the SAHE, other spin-charge conversion processes allow to generate  $J_s$  with a variety of spin-polarization vectors such as spin precession process [8,9]. Stimulated by these theoretical predictions, many experimental works have recently reported the generation of  $J_s$  in the FM bulks or at the FM interfaces [15].

For developing a spin Hall material, it is a guide to exploit the topological features in an electronic band structure [28,29].  $\text{Co}_3\text{Sn}_2\text{S}_2$  (CSS) is one of the shandite compounds, and has attracted much attention as a promising candidate for magnetic Weyl semimetals [30–37]. Thanks to its specific band structure, CSS exhibits half metallicity and huge AHE below the ferromagnetic phase transition temperature

\*takeshi.seki@tohoku.ac.jp

Published by the American Physical Society under the terms of the [Creative Commons Attribution 4.0 International license](https://creativecommons.org/licenses/by/4.0/). Further distribution of this work must maintain attribution to the author(s) and the published article's title, journal citation, and DOI.

( $T_C$ ) that was reported to be  $\sim 175$  K in bulk [38–41]. One may expect that the ferromagnetic CSS shows the highly efficient spin-charge conversion. The paramagnetic CSS above  $T_C$  is also an attractive candidate for improvement of the spin-charge conversion efficiency by carefully considering its band structure. Our group has already demonstrated that the Fermi-level tuning of the paramagnetic CSS by elemental doping is very effective to obtain the enhanced spin Hall conductivity at room temperature [42]. Although our previous study suggests that the paramagnetic CSS family is a promising spin Hall material, no one has understood yet how the ferromagnetic phase transition accompanying with the variation of electronic band affects the spin-charge conversion process in the case of the CSS. For example, it is unclear if the spin Hall effect for the CSS is enhanced in the vicinity of  $T_C$  as shown in the previous studies for other ferromagnets [43,44]. This is an essential question to understand the spin-charge conversion process in the magnetic topological materials.

In this paper, the temperature ( $T$ ) dependence of spin-charge conversion in the CSS thin film is investigated by measuring the spin-torque ferromagnetic resonance (ST-FMR) for the trilayer consisting of CSS/Cu/Co<sub>20</sub>Fe<sub>60</sub>B<sub>20</sub> (CFB). By carefully analyzing the field angular dependence of ST-FMR signal, we examine the influence of ferromagnetic phase transition on the spin-charge conversion efficiency, and discuss the major process of spin-charge conversion in the ferromagnetic CSS. In addition, we study the spin-charge conversion process of CSS based on the effective tight-binding model. This paper is composed of the following sections. Section II describes the experimental procedures including the film preparation and the details of ST-FMR measurement method. Section III is devoted to the experimental results and discussion, and is divided into five subsections: temperature dependence of Hall effect and magnetoresistance, spin-torque ferromagnetic resonance spectra, quantitative analysis of spin torque, enhanced spin-charge conversion efficiency for ferromagnetic CSS, and discussion. In Sec. IV, theoretical calculation is shown. Finally, the conclusion is given in Sec. V.

## II. EXPERIMENTAL PROCEDURE

The 15-nm-thick CSS layer was prepared on the Al<sub>2</sub>O<sub>3</sub> (0001) substrate by radio-frequency magnetron sputtering. A CSS layer and a Si-O capping layer were deposited at a substrate temperature of 400 °C under an Ar gas of 0.5 Pa. Subsequently, *in situ* annealing was performed at 800 °C in a vacuum to promote the crystallization of CSS. The Si-O capping layer was used to prevent reevaporation during the annealing. The *c*-axis oriented growth of CSS was confirmed by x-ray diffraction measurement, which was reported in Ref. [42]. The CSS/Si-O film was set into the Ar ion milling chamber to remove the Si-O capping layer. During this ion milling process, the surface of CSS layer was also etched, and the designed CSS layer thickness was reduced to 9.8 nm. After the removal of Si-O layer, subsequently Cu (1.8 nm)/CFB (2 nm)/Al-O (5 nm) were deposited at room temperature by employing the ion beam sputtering system.

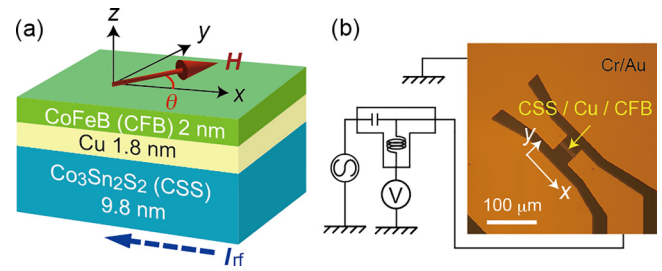


FIG. 1. (a) Schematic illustration of thin-film structure, and (b) optical microscope image of coplanar waveguide (CPW) device together with the measurement circuit for spin-torque ferromagnetic resonance (ST-FMR). The magnetic field ( $H$ ) was applied in the film plane with the angle of  $\theta$ , and the rf current ( $I_{rf}$ ) was applied along the  $x$  direction.

For the ST-FMR measurement, the CSS/Cu/CFB/Al-O stack was patterned into a rectangular-shaped element with  $10\text{-}\mu\text{m}$  width ( $w$ ) and  $40\text{-}\mu\text{m}$  length, and the Au electrodes of coplanar waveguide were fabricated through the use of photolithography and Ar ion milling. The ST-FMR measurement was carried out with the setup employed in the previous studies [12,17,45,46]. As illustrated in Fig. 1(a), the radio-frequency (rf) current ( $I_{rf}$ ) was applied along the  $x$  direction, and the in-plane angle of external magnetic field ( $H$ ) was set at  $\theta$  from the  $x$  direction. The rf power of 15 dBm was applied from a signal generator [Fig. 1(b)], inducing an oscillating transverse magnetic field in the  $y$  direction. The excitation frequency ( $f$ ) of  $I_{rf}$  was varied in the range from 6 to 16 GHz. The device resistance [ $R(t)$ ] oscillated through the anisotropic magnetoresistance (AMR) and/or giant magnetoresistance (GMR) effect at the condition that  $H$  matched the resonance field ( $H_{res}$ ). As a result, applied  $I_{rf}(t) [= I \cos(2\pi ft)]$  and oscillating  $R(t) [\propto \cos(2\pi ft)]$  generated a rectification dc voltage ( $V_{dc}$ ), which was detected by a lock-in amplifier. In addition to the coplanar waveguide device, the Hall devices were prepared for measuring the temperature dependence of the longitudinal resistance ( $R_{xx}$ ) and the transverse resistance ( $R_{yx}$ ). The coplanar waveguide device and the Hall device were fabricated on the identical substrate. The ST-FMR spectra were measured for the coplanar waveguide device employing the temperature-variable rf-compatible probe station. The maximum in-plane  $|H|$  of the probe station was 6 kOe. The values of  $R_{xx}$  and  $R_{yx}$  for the Hall device were measured with the superconducting magnet allowing to increase  $H$  up to 70 kOe along in-plane and out-of-plane directions.

The magnetic properties of the blanket films were characterized using a superconducting quantum interference device magnetometer.

## III. EXPERIMENTAL RESULTS AND DISCUSSION

### A. Temperature dependence of Hall effect and magnetoresistance

Figure 2(a) shows  $R_{yx}$  versus out-of-plane magnetic field ( $H_z$ ) for the Hall device measured at  $T = 300, 200, 150,$  and  $100$  K. The linear variation without hysteresis in the of  $R_{yx}$ - $H_z$  curves is observed at  $T = 300$  and  $200$  K. These

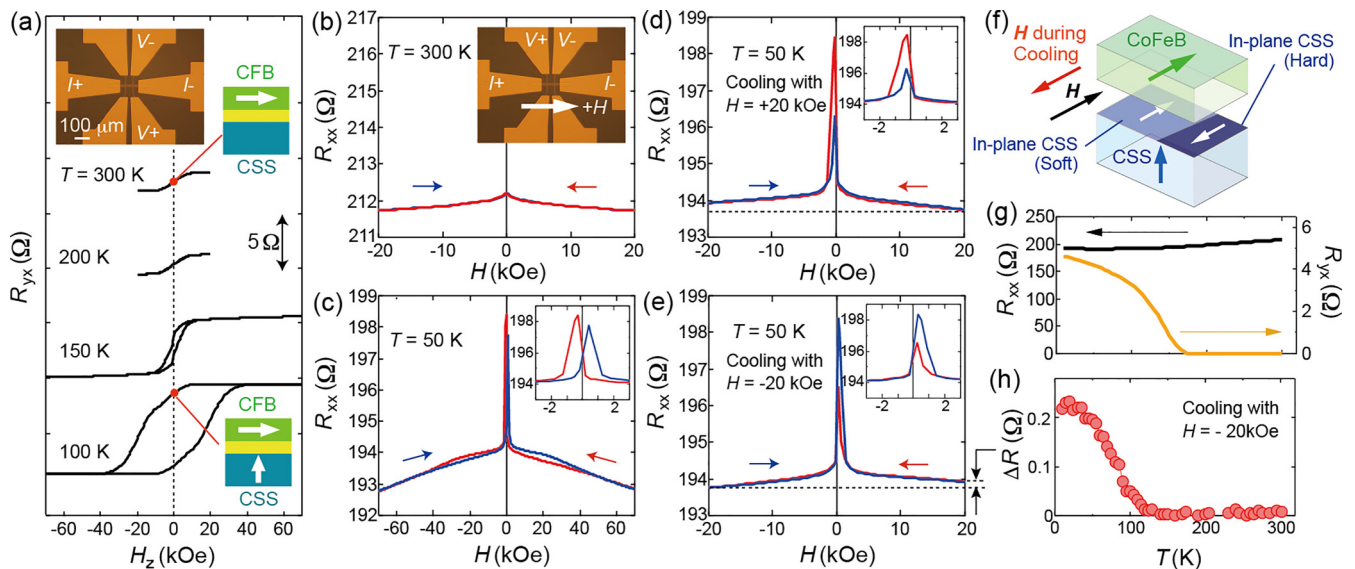


FIG. 2. (a) Transverse resistance ( $R_{yx}$ ) vs out-of-plane magnetic field ( $H_z$ ) for the Hall device measured at  $T = 300, 200, 150,$  and  $100$  K. Insets display the optical microscope image with current and voltage probes and the schematic illustrations of magnetization configurations. The  $R_{yx}$ - $H_z$  curves were vertically shifted for clarity. (b) Magnetoresistance (MR) curve measured at  $T = 300$  K. The longitudinal resistance ( $R_{xx}$ ) was measured using the four-probe method, and the in-plane magnetic field ( $H$ ) was applied along the channel of Hall device as shown in the inset. (c) Full MR curve measured at  $50$  K with  $H$  applied in the range of  $\pm 70$  kOe, and (d) minor MR curve with  $H$  applied in the range of  $\pm 20$  kOe. For both measurements, the device was cooled down to  $50$  K under the application of  $H = +20$  kOe. (e) Minor MR curve, in which the device was cooled down with  $H = -20$  kOe applied. Red (blue) arrow denotes the field-sweep direction from positive (negative) to negative (positive). In (c), (d), and (e), the MR curves enlarged at low  $H$  regions are shown as the insets. Black dotted lines in (d) and (e) compare the values of  $R_{xx}$  at  $+20$  and  $-20$  kOe, indicating that there exists the difference in  $R_{xx}$  between  $H = +20$  and  $-20$  kOe, which was defined as  $\Delta R$ . (f) Schematic illustration of possible magnetic structures in CFB and CSS when  $H$  (denoted by black arrow) was applied opposite to the magnetic field during cooling the device (denoted by red arrow), which corresponds to the magnetization configuration in the minor MR curve. (g)  $R_{xx}$  and  $R_{yx}$  as a function of  $T$ . (h)  $\Delta R$  as a function of  $T$ , in which the device was cooled down with  $H = -20$  kOe applied.

small changes in  $R_{yx}$  originate from the AHE of CFB layer. The CFB layer is in-plane magnetized at  $H_z = 0$  Oe and becomes out-of-plane magnetized as  $H_z$  is increased up to  $10$  kOe. When  $T$  was reduced to  $150$  K, the AHE of CSS layer contributes to  $R_{yx}$ . The further reduction of  $T$  to  $100$  K leads to the clear hysteretic behavior and the large remanent  $R_{yx}$  at  $H_z = 0$  Oe because of the out-of-plane spontaneous magnetization of CSS. These results indicate that  $T_C$  of the present CSS layer exists between  $150$  and  $200$  K.

Employing the identical device,  $R_{xx}$  versus in-plane  $H$  was measured. This corresponds to the magnetoresistance (MR) curve measurement. Figure 2(b) displays the MR curve measured at  $T = 300$  K, where the red (blue) curve denotes the MR curve under the in-plane  $H$  sweeping from positive (negative) to negative (positive). A small but sharp change in  $R_{xx}$  at low  $H$  and the following gradual  $R_{xx}$  variation are observed as  $H$  is increased, which come from the AMR and the forced effect, respectively, of the CFB layer. When  $T$  is reduced down to  $50$  K, the large resistance change is observed at low  $H$  [Fig. 2(c)]. The inset of Fig. 2(c) shows the corresponding MR curve enlarged at the low  $H$  region. This is attributable to the GMR effect due to the change in the relative configuration of in-plane magnetization components between CSS and CFB, although the CSS is mostly magnetized along the out-of-plane direction, which will be explained later. One of the remarkable features for the MR

curves at  $T < T_C$  is that the exchange-biased-like behavior, i.e., an asymmetric MR curve with respect to the zero magnetic field is observed if the applied in-plane  $H$  is insufficient for fully saturating the in-plane component of CSS. This is because the CSS layer possesses the high magnetic anisotropy and the resultant large switching field. Figures 2(d) and 2(e) correspond to the minor MR curves at  $T = 50$  K measured with the narrow  $H$  sweep ( $\pm 20$  kOe), where the in-plane  $H = +20$  and  $-20$  kOe, respectively, were applied during the device cooling from  $T = 300$  to  $50$  K. In Fig. 2(d) with  $+20$  kOe field cooling, the positive exchange-bias-like field, i.e., the sharp resistance change only in the negative  $H$  region (see the inset) is observed, whereas the negative exchange-bias-like field is induced for the case of Fig. 2(e) with  $-20$  kOe field cooling. As seen in the AHE hysteresis of Fig. 2(a), the CSS is mostly magnetized along the out-of-plane direction. Nevertheless, the GMR effect accompanied by the exchange-biased-like behavior appears when the in-plane  $H$  was applied. Considering these facts, the in-plane magnetized CSS exists near the interface, and a part of in-plane magnetized CSS shows soft magnetic behavior and the other shows hard magnetic behavior. The appearance of in-plane magnetization component may be due to the CSS damaged during the Ar ion milling process. In addition, the results of minor MR curves [Figs. 2(d) and 2(e)] indicate that the direction of magnetic field cooling determines the initially magnetized direction for the hard magnetic CSS. The

magnetic moments in the soft magnetic CSS are easily switched by  $H$ , but are coupled to the hard magnetic phase, resulting in the exchange-bias-like behavior. Figure 2(f) schematically illustrates possible magnetic structures in CFB and CSS. The coexistence of in-plane magnetized soft and hard magnetic CSS is one scenario to explain the observed MR curves. One may think that the exchange-bias-like behavior is due to the appearance of antiferromagnetic (AFM) phase [47] or geometric frustration intrinsic to the kagome network of magnetic ions [48]. According to the paper reporting the AFM phase [47], the AFM phase appears in the limited  $T$  region around  $T_C$ . Figure 2(g) displays the  $T$  dependence of  $R_{xx}$  and  $R_{yx}$  and Fig. 2(h) displays the  $T$  dependence of  $\Delta R$  defined as the difference between  $R_{xx}$  at  $H = +20$  and  $-20$  kOe in the minor MR curve [see Fig. 2(e)]. From these temperature dependences, we point out the following two results. First, the  $T$  dependence of  $R_{yx}$  suggests that  $T_C$  for the present CSS is  $\sim 170$  K. Second,  $\Delta R$  is observed from around 100 K to even at 10 K. These facts indicate that the exchange-bias-like mechanism is maintained at  $T$  much lower than the limited  $T$  region of AFM reported in Ref. [46], and we consider that the AFM phase is not responsible for the exchange-bias-like behavior observed in this study. On the contrary, it was reported that the geometric frustration appears at  $T < T_G = 125$  K at which a spin-glass phase is considered to be formed [48]. As shown in Fig. 2(h),  $\Delta R$  becomes remarkable at  $T$  below  $T_C$ . This result may suggest the contribution of geometric frustration. In order to explain the shape of MR curve, however, the phase pinning the soft magnetic CSS should possess the spontaneous magnetization. Considering this point, we currently think that not the geometric frustration but the hard magnetic phase of CSS gives rise to the exchange-bias-like MR shift for the present samples. Here, let us summarize the possible three magnetic phases: in-plane magnetized soft magnetic CSS, in-plane magnetized hard magnetic CSS, and out-of-plane magnetized hard magnetic CSS. At present, we think that the in-plane magnetized soft magnetic CSS resulted from the damage (atomic disordering) during the Ar ion milling process. On the contrary, there is a possibility that the in-plane magnetized hard magnetic CSS is the in-plane component of CSS that mostly possesses the out-of-plane magnetization (see Appendix A). The coplanar waveguide devices for the ST-FMR measurement exhibited the  $T$  dependence of MR effect similar to those observed for the Hall devices, which is given in Appendix B.

### B. Spin-torque ferromagnetic resonance spectra

Figures 3(a) and 3(b) display  $V_{dc}$  as a function of  $H$  measured at  $T = 300$  and 80 K, respectively, by varying the in-plane field angle of  $\theta$ .  $f$  was fixed at 16 GHz. The results for  $T = 300$  K show clear ST-FMR at  $\theta \neq 0^\circ, 90^\circ, 180^\circ$ , and  $270^\circ$ . The single-peak spectral shapes indicate that the resonance spectra are composed of ferromagnetic resonance for the single ferromagnet. Since the CSS is paramagnetic at  $T = 300$  K, the ST-FMR originates from the magnetization dynamics of the CFB layer induced by spin torque. When  $T$  is reduced to 80 K, the drastic change appears in the ST-FMR spectra. In addition to the increase in the magnitude of  $V_{dc}$ , the most apparent difference from  $T = 300$  K is its

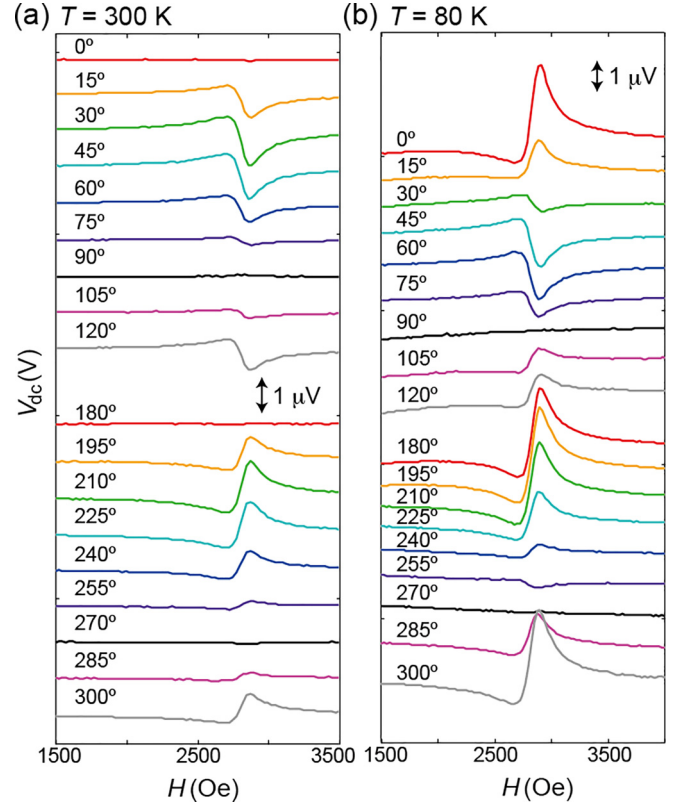


FIG. 3. ST-FMR spectra measured at (a)  $T = 300$  K and (b) 80 K, in which the excitation frequency ( $f$ ) was fixed at 16 GHz while  $\theta$  was varied. For clarity, the spectra were shifted vertically.

field angular dependence. For example, the nonzero  $V_{dc}$  is obtained at  $\theta = 0^\circ$  and  $180^\circ$  for  $T = 80$  K. It is noted that the single-resonance peaks are observed even at  $T = 80$  K, where the CSS becomes ferromagnetic. As discussed later in the plot of  $H_{res}$  versus  $f$ , the ST-FMR signals at  $T = 80$  K come from only the CFB layer as well as the result at  $T = 300$  K. This is because of large perpendicular magnetic anisotropy (PMA) and the resultant high  $H_{res}$  of ferromagnetic CSS.

### C. Quantitative analysis of spin torque

In order to quantitatively analyze the spin torque acting on the CFB layer, the ST-FMR spectra are fitted using the summation of Lorentzian and anti-Lorentzian functions given by  $V_{dc} = V_S(\theta)f_L(H) + V_A(\theta)f_{AL}(H)$ , respectively, in which  $f_L(H) = (\Delta H/2)^2 / [(H_{res} - H)^2 + (\Delta H/2)^2]$  and  $f_{AL}(H) = (\Delta H/2)(H_{res} - H) / [(H_{res} - H)^2 + (\Delta H/2)^2]$ , and  $\Delta H$  represents the resonance linewidth. In general,  $V_S$  is mostly proportional to the dampinglike torque ( $\tau_x^0$ ) whereas  $V_A$  is mostly proportional to the fieldlike torque ( $\tau_y^0$ ) including the Oersted field contribution [45,46]. As explained later in detail, however, we also take into account the rectification effect due to the resistance change coming from out-of-plane magnetization, which gives rise to the phase shift in the effective torque direction by  $\pi/2$ . Figure 4(a) is the spectrum fitted with  $f_L(H)$  and  $f_{AL}(H)$  measured at  $T = 80$  K,  $\theta = 0^\circ$ , and  $f = 16$  GHz. The numerical fitting allows to decompose the spectrum well into the Lorentzian and anti-Lorentzian

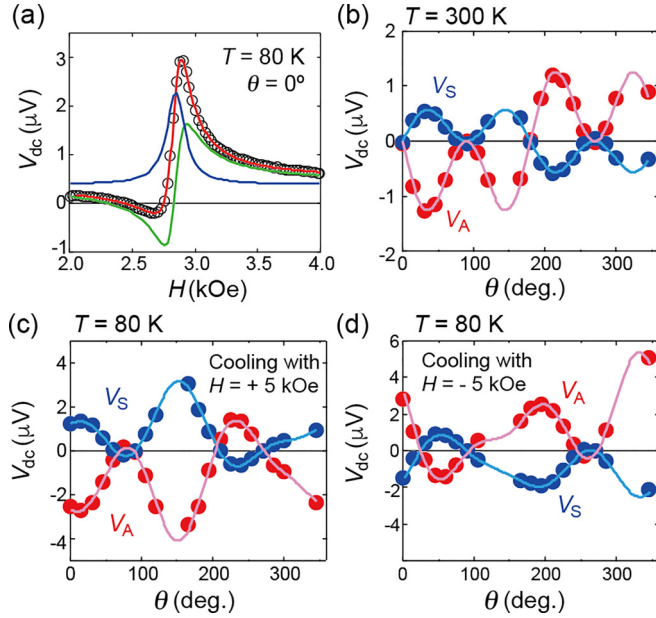


FIG. 4. (a) Fitting curves for the ST-FMR spectrum obtained at  $T = 80$  K,  $\theta = 0^\circ$ , and  $f = 16$  GHz, where  $T$  was reduced under the application of  $H = +5$  kOe along  $\theta = 45^\circ$ . (b)  $\theta$  dependence of detected dc voltage ( $V_{dc}$ ) measured at  $T = 300$  K and  $f = 16$  GHz. (c), (d)  $\theta$  dependence of  $V_{dc}$  measured at 80 K and  $f = 16$  GHz, in which  $T$  was reduced under the application of (c)  $H = +5$  kOe and (d)  $-5$  kOe along  $\theta = 45^\circ$ . Blue and red marks represent the experimental values of symmetric ( $V_S$ ) and antisymmetric components ( $V_A$ ), respectively, and the solid curves represent the fitting results.

components (blue and green curves). Consequently,  $V_S$  and  $V_A$  are evaluated.

The  $\theta$  dependence of  $V_S$  and  $V_A$  for  $T = 300$  K is plotted in Fig. 4(b), where  $f$  was fixed at 16 GHz. At  $T = 300$  K the CSS is paramagnetic, and  $V_{dc}$  comes from the oscillating  $R(t)$  through the AMR effect of CFB. Here, the in-plane angle of magnetization vector of CFB ( $\mathbf{M}^{\text{CFB}}$ ) is defined as  $\varphi^{\text{CFB}}$ , and it is assumed that  $\mathbf{M}^{\text{CFB}}$  follows  $\mathbf{H}$ , i.e.,  $\varphi^{\text{CFB}} = \theta$ .  $V_{dc}$  originating from AMR ( $V_{dc}^{\text{AMR}}$ ) has the following  $\theta$  dependence:

$$V_{dc}^{\text{AMR}} \propto \sin 2\theta \left[ f_L(H)\tau_X^0 + \frac{\gamma H_{YY}}{\omega_0} f_{AL}(H)\tau_Y^0 \right], \quad (2)$$

where  $\omega_0$  and  $\gamma$  are the resonance frequency and the gyromagnetic ratio, respectively.  $H_{YY}$  is given by  $H_{YY} = H + 4\pi M^{\text{CFB}}$ . The detailed derivations are given in Appendix C. At the condition of  $T = 300$  K, we assume that  $\tau_X^0$  corresponds to the torque coming from spin Hall effect ( $\tau_{\text{SHE}}$ ) in the paramagnetic CSS while  $\tau_Y^0$  is mostly the current-induced Oersted field torque ( $\tau_{\text{Oe}}$ ). Here,  $\tau_Y^0 \sim \tau_{\text{Oe}}$  is assumption for the present analysis. For the strict evaluation, we should take into account the fieldlike torques such as Rashba-Edelstein effect and separate them from  $\tau_{\text{Oe}}$ . We are yet to do the separation, and that is one of the remaining tasks for the future study.  $\tau_{\text{SHE}}$  and  $\tau_{\text{Oe}}$  are expressed as

$$\tau_{\text{SHE}} = \alpha_{\text{SH}} \frac{\gamma \hbar}{2eM_s d^{\text{CFB}} d^{\text{CSS}}} (I_{\text{rf}} \eta_{\text{CSS}}) \cos \theta, \quad (3)$$

and

$$\tau_{\text{Oe}} = \frac{\gamma \mu_0}{2w} (I_{\text{rf}} \eta_{\text{Cu+CSS}}) \cos \theta, \quad (4)$$

where  $\mu_0$  is the permeability in vacuum,  $M_s$  is the saturation magnetization of CFB, and  $d^{\text{CFB(CSS)}}$  is the thickness of CFB (CSS) layer.  $\eta_{\text{CSS}}$  ( $\eta_{\text{Cu+CSS}}$ ) is the ratio of current flowing in the CSS layer (Cu and CSS layers). From Eqs. (2)–(4), one may expect that  $V_S$  and  $V_A$  follow the  $\sin 2\theta \cos \theta$  dependence. The experimental data in Fig. 4(b) are well fitted by the  $\sin 2\theta \cos \theta$  function as in the cases of previous study [46].

Figures 4(c) and 4(d) show the  $\theta$  dependence of  $V_S$  and  $V_A$  for  $T = 80$  K, where the device was cooled down to 80 K under the application of  $H = +5$  and  $-5$  kOe, respectively, along  $\theta = 45^\circ$ . The  $\theta$  dependence of  $V_S$  and  $V_A$  for  $T = 80$  K is totally different from that for  $T = 300$  K. Since the CSS is ferromagnetic at  $T = 80$  K,  $V_{dc}$  appears through the AMR effect and/or GMR effect. Based on the experimental fact that the in-plane MR curves exhibit exchange-bias-like behavior (Fig. 2), we consider that the CSS layer is divided into three regions: in-plane soft magnetic CSS, in-plane hard magnetic CSS, and out-of-plane hard magnetic CSS as illustrated in Fig. 2(f). The magnetization vector of in-plane soft magnetic CSS ( $\mathbf{M}^{\text{CSS,soft}}$ ) easily follows  $\mathbf{H}$  as well as  $\mathbf{M}^{\text{CFB}}$ . The MR curve shown in Fig. 2(c) suggests  $\mathbf{M}^{\text{CSS,soft}}$  and  $\mathbf{M}^{\text{CFB}}$  are aligned along  $\mathbf{H}$  at  $|H| > 1500$  Oe. On the other hand, the magnetization vector of in-plane hard magnetic CSS ( $\mathbf{M}^{\text{CSS,hard}}$ ) is fixed at  $\theta = 45^\circ$  because of the field cooling. The in-plane angles of  $\mathbf{M}^{\text{CSS,soft}}$  and  $\mathbf{M}^{\text{CSS,hard}}$  are defined as  $\varphi^{\text{CSS,soft}}$  and  $\varphi^{\text{CSS,hard}}$ , respectively. The out-of-plane hard magnetic CSS ( $\mathbf{M}^{\text{CSS,oop}}$ ) is also not affected by  $\mathbf{H}$  because of the strong PMA. In the above situation, we need to consider the following possible sources generating the torque: (i) SHE in the ferromagnetic CSS, (ii) SAHE originating from  $\mathbf{M}^{\text{CSS,soft}}$  and/or  $\mathbf{M}^{\text{CSS,hard}}$ , (iii) spin precession by  $\mathbf{M}^{\text{CSS,soft}}$ ,  $\mathbf{M}^{\text{CSS,hard}}$ , and/or  $\mathbf{M}^{\text{CSS,oop}}$ , which is called the spin precession torque (SPT) [8,9], and (iv) Oersted field. The symmetries of  $\tau_X^0$  originating from SHE, SAHE, and spin precession are explained in Appendix D. Since  $\mathbf{M}^{\text{CSS,soft}}$  and  $\mathbf{M}^{\text{CFB}}$  follow  $\mathbf{H}$  in the  $H$  region for the ST-FMR measurement,  $\varphi^{\text{CSS,soft}} = \varphi^{\text{CFB}} = \theta$ . This case leads to zero  $\tau_X^0$  coming from SAHE because it is proportional to  $\sin \varphi^{\text{CSS,soft}} \sin(\varphi^{\text{CFB}} - \varphi^{\text{CSS,soft}})$ . Therefore, only SAHE from  $\mathbf{M}^{\text{CSS,hard}}$  is taken into account for the present experiment. Since all the angular dependences of SHE, SAHE, and SPT involve the terms of the first order of  $\theta$ , unfortunately, the current ST-FMR measurement condition and the numerical fitting do not enable us to separate the contributions from SHE in the ferromagnetic CSS and SAHE originating from  $\mathbf{M}^{\text{CSS,hard}}$ . In this study, thus, the SHE and the SAHE are evaluated together as a “spin Hall torque (SHT).”  $\mathbf{M}^{\text{CSS,oop}}$  does not contribute to the SAHE because  $\mathbf{M}^{\text{CSS,oop}}$  does not generate the anomalous Hall current along the  $z$  direction. The spin precession due to the out-of-plane magnetized  $\mathbf{M}^{\text{CSS,oop}}$  contributes to  $\tau_X^0$  while that due to the in-plane magnetized  $\mathbf{M}^{\text{CSS,soft}}$  and  $\mathbf{M}^{\text{CSS,hard}}$  gives rise to  $J_s$  with the out-of-plane polarized spin, which acts as  $\tau_Y^0$ . Then, the SPT from  $\mathbf{M}^{\text{CSS,soft}}$  and  $\mathbf{M}^{\text{CSS,hard}}$  (ipSPT) is not regarded as a source generating  $\tau_X^0$ . It is noted that the SPT from  $\mathbf{M}^{\text{CSS,soft}}$  possesses the same symmetry as that for  $\tau_{\text{Oe}}$ , which does

TABLE I. Estimated values of  $V_S^{\text{SHT,GMR}}$ ,  $V_S^{\text{SPT,GMR}}$ ,  $V_S^{\text{SHT,AMR}}$ ,  $V_S^{\text{SPT,AMR}}$ ,  $V_S^{\text{Oe,oopGMR}}$ ,  $V_S^{\text{ipSPT,oopGMR}}$ , and  $\varphi^{\text{CSS,hard}}$  by numerical fit using Eq. (6) to in-plane field angular  $\theta$  dependence of  $V_S$  for  $T = 80$  K, in which the device was cooled with  $H = +5$  and  $-5$  kOe along  $\theta = 45^\circ$ .

	$V_S^{\text{SHT,GMR}} (\mu\text{V})$	$V_S^{\text{SPT,GMR}} (\mu\text{V})$	$V_S^{\text{SHT,AMR}} (\mu\text{V})$	$V_S^{\text{SPT,AMR}} (\mu\text{V})$	$V_S^{\text{Oe,oopGMR}} (\mu\text{V})$	$V_S^{\text{ipSPT,oopGMR}} (\mu\text{V})$	$\varphi^{\text{CSS,hard}} (^\circ)$
Cooling $H = +5$ kOe	$2.29 \pm 0.05$	$0.04 \pm 0.06$	$1.24 \pm 0.05$	$0.05 \pm 0.06$	$-0.39 \pm 0.03$	$0.00 \pm 0.03$	$45 \pm 1$
Cooling $H = -5$ kOe	$2.22 \pm 0.05$	$0.02 \pm 0.05$	$1.05 \pm 0.05$	$0.08 \pm 0.05$	$0.20 \pm 0.03$	$0.00 \pm 0.03$	$228 \pm 1$

not allow us to separate them. In this study, we analyze  $\tau_Y^0$  with  $\tau_{\text{Oe}}$  including the contribution of SPT from  $\mathbf{M}^{\text{CSS,soft}}$ . Here, using the unit vector of CFB magnetization ( $\mathbf{m}^{\text{CFB}}$ ) and the coordinates given in Appendix C we summarize the following four torque mechanisms:  $\tau_{\text{Oe}}$ ,  $\mathbf{m}^{\text{CFB}} \times \mathbf{e}_y = \cos\theta \mathbf{e}_x$ , SHT ( $\tau_{\text{SH}}$ ),  $\mathbf{m}^{\text{CFB}} \times (\mathbf{e}_y \times \mathbf{m}^{\text{CFB}}) = \cos\theta \mathbf{e}_x$ , SPT ( $\tau_{\text{SP}}$ ) due to  $\mathbf{M}^{\text{CSS,OOP}}$ ,  $\mathbf{m}^{\text{CFB}} \times [(\mathbf{m}^{\text{CSS,OOP}} \times \mathbf{e}_y) \times \mathbf{m}^{\text{CFB}}] = \sin\theta \mathbf{e}_x$ , and  $\tau_{\text{SP}}$  due to  $\mathbf{M}^{\text{CSS,hard}}$ ,  $\mathbf{m}^{\text{CFB}} \times [(\mathbf{m}^{\text{CSS,hard}} \times \mathbf{e}_y) \times \mathbf{m}^{\text{CFB}}] = \cos\varphi^{\text{CSS,hard}} \mathbf{e}_x$ .

In addition to these various torques, we need to consider three MR effects responsible for the rectification: AMR effect, GMR effect due to the in-plane hard magnetic CSS, and GMR effect due to the out-of-plane magnetized hard magnetic CSS

(oop-GMR).  $V_{\text{dc}}$  originating from in-plane GMR ( $V_{\text{dc}}^{\text{GMR}}$ ) has the following  $\theta$  dependence:

$$V_{\text{dc}}^{\text{GMR}} \propto -\sin(\theta - \varphi^{\text{CSS,hard}}) \left[ f_L(H) \tau_X^0 + \frac{\gamma H_{YY}}{\omega_0} f_{AL}(H) \tau_Y^0 \right]. \quad (5)$$

On the other hand, the rectification by oop-GMR does not show the  $\theta$  dependence and leads to only the phase shift in the effective torque direction by  $\pi/2$ .

These 4 torques and 3 MR effects lead to the 12 combinations for the generation processes of  $V_{\text{dc}}$ . Then, the  $\theta$  dependence of  $V_{\text{dc}}$  is expressed as

$$\begin{aligned} V_{\text{dc}} = & \left[ -V_S^{\text{SHT,GMR}} \sin(\theta - \varphi^{\text{CSS,hard}}) \cos\theta - V_S^{\text{SPT,GMR}} \sin(\theta - \varphi^{\text{CSS,hard}}) \sin\theta \right. \\ & + V_S^{\text{SHT,AMR}} \sin 2\theta \cos\theta + V_S^{\text{SPT,AMR}} \sin 2\theta \sin\theta + V_S^{\text{Oe,oopGMR}} \cos\theta + V_S^{\text{ipSPT,oopGMR}} \left. \right] f_L(H) \\ & + \left[ -V_A^{\text{Oe,GMR}} \sin(\theta - \varphi^{\text{CSS,hard}}) \cos\theta + V_A^{\text{Oe,AMR}} \sin 2\theta \cos\theta + V_A^{\text{SHT,oopGMR}} \cos\theta + V_A^{\text{SPT,oopGMR}} \sin\theta \right. \\ & \left. + V_A^{\text{ipSPT,AMR}} \sin 2\theta + V_A^{\text{ipSPT,GMR}} \sin(\theta - \varphi^{\text{CSS,hard}}) \right] f_{AL}(H). \quad (6) \end{aligned}$$

Equation (6) enables us to well fit the  $\theta$  dependence of  $V_S$  and  $V_A$  for  $T = 80$  K as shown in Figs. 4(c) and 4(d). Table I (Table II) summarizes the values of  $V_S^{\text{SHT,GMR}}$ ,  $V_S^{\text{SPT,GMR}}$ ,  $V_S^{\text{SHT,AMR}}$ ,  $V_S^{\text{SPT,AMR}}$ ,  $V_S^{\text{Oe,oopGMR}}$ ,  $V_S^{\text{ipSPT,oopGMR}}$ , and  $\varphi^{\text{CSS,hard}}$  ( $V_A^{\text{Oe,GMR}}$ ,  $V_A^{\text{Oe,AMR}}$ ,  $V_A^{\text{SHT,oopGMR}}$ ,  $V_A^{\text{SPT,oopGMR}}$ ,  $V_A^{\text{ipSPT,AMR}}$ , and  $V_A^{\text{ipSPT,GMR}}$ ) obtained by the numerical fit for the device cooled with  $H = +5$  and  $-5$  kOe. The similar values are obtained for each parameter between two field-cooling conditions, e.g.,  $V_S^{\text{SHT,GMR}} = 2.29 \pm 0.05$  and  $2.22 \pm 0.05$   $\mu\text{V}$  for the cooling with  $H = +5$  and  $-5$  kOe, respectively. On the contrary,  $\varphi^{\text{CSS,hard}}$  clearly depends on the field-cooling condition, i.e.,  $\varphi^{\text{CSS,hard}} \sim 45^\circ$  and  $228^\circ$  for the field-cooling conditions with  $H = +5$  and  $-5$  kOe, respectively. These  $\varphi^{\text{CSS,hard}}$  values depending on the field-cooling condition are consistent with the results of MR measurement indicating that the  $H$  direction during the cooling determines the initial state of  $\mathbf{M}^{\text{CSS,hard}}$ . Although the fitting to the  $\theta$  dependence of  $V_S$  gives the parameters with small errors,  $V_A^{\text{SHT,oopGMR}}$ ,

$V_A^{\text{SPT,oopGMR}}$ , and  $V_A^{\text{ipSPT,GMR}}$  obtained from the  $\theta$  dependence of  $V_A$  are the small values with very large errors. The low accuracy of fitting for these coefficients of  $V_A$  comes from that these have similar trigonometric functions. Here, let us examine whether  $V_A^{\text{SHT,oopGMR}}$ ,  $V_A^{\text{SPT,oopGMR}}$ , and  $V_A^{\text{ipSPT,GMR}}$  are negligibly small or not. Comparing between  $V_S^{\text{Oe,oopGMR}}$  and  $V_A^{\text{Oe,GMR}}$ , the voltage coming from the out-of-plane GMR is one order of magnitude smaller than that from the in-plane GMR, suggesting the small contribution of out-of-plane GMR. Also, the very small  $V_A^{\text{ipSPT,AMR}}$  implies the negligible contribution of SPT coming from the in-plane CSS. Considering these facts,  $V_A^{\text{SHT,oopGMR}}$ ,  $V_A^{\text{SPT,oopGMR}}$ , and  $V_A^{\text{ipSPT,GMR}}$  are indeed small; then, out-of-plane GMR and SPT coming from the in-plane CSS are not major processes for the generation of  $V_{\text{dc}}$ . Hereafter, we consider only four processes for  $V_S$ : SHT+GMR, SPT+GMR, SHT+AMR, and SPT+AMR

From the values shown in Tables I and II, the values of  $V_S / V_A$  are calculated, which are given in Table III. It should

TABLE II. Estimated values of  $V_A^{\text{Oe,GMR}}$ ,  $V_A^{\text{Oe,AMR}}$ ,  $V_A^{\text{SHT,oopGMR}}$ ,  $V_A^{\text{SPT,oopGMR}}$ ,  $V_A^{\text{ipSPT,AMR}}$ , and  $V_A^{\text{ipSPT,GMR}}$  by numerical fit using Eq. (6) to in-plane field angular  $\theta$  dependence of  $V_A$  for  $T = 80$  K, in which the device was cooled with  $H = +5$  and  $-5$  kOe along  $\theta = 45^\circ$ .

	$V_A^{\text{Oe,GMR}} (\mu\text{V})$	$V_A^{\text{Oe,AMR}} (\mu\text{V})$	$V_A^{\text{SHT,oopGMR}} (\mu\text{V})$	$V_A^{\text{SPT,oopGMR}} (\mu\text{V})$	$V_A^{\text{ipSPT,AMR}} (\mu\text{V})$	$V_A^{\text{ipSPT,GMR}} (\mu\text{V})$
Cooling $H = +5$ kOe	$-3.51 \pm 0.07$	$-1.65 \pm 0.13$	$0.16 \pm (2 \times 10^4)$	$-0.39 \pm (2 \times 10^4)$	$-0.01 \pm 0.06$	$0.45 \pm (3 \times 10^4)$
Cooling $H = -5$ kOe	$-3.67 \pm 0.08$	$-2.40 \pm 0.11$	$0.02 \pm (2 \times 10^4)$	$0.38 \pm (2 \times 10^4)$	$-0.18 \pm 0.05$	$-0.55 \pm (3 \times 10^4)$

TABLE III. Calculated values of  $V_S/V_A$  for the processes of SHT+GMR, SPT+GMR, SHT+AMR, and SPT+AMR at  $T = 80$  K, in which the device was cooled with  $H = +5$  kOe and  $-5$  kOe along  $\theta = 45^\circ$ .

	SHT+ GMR	SPT+ GMR	SHT+ AMR	SPT+ AMR
Cooling $H = +5$ kOe	-0.65	-0.01	-0.75	-0.03
Cooling $H = -5$ kOe	-0.60	-0.01	-0.44	-0.03

be noted here that the values of  $V_S/V_A$  originating from SPT are much smaller than that of SHT, suggesting the negligible contribution of spin precession process to the spin torque in the present CSS/Cu/CFB trilayer. In other words, the SHT is the major spin torque acting on the CFB magnetization. In the next section, we discuss the spin-charge conversion efficiency using the  $V_S/V_A$  values originating from the SHT.

#### D. Enhanced spin-charge conversion efficiency for ferromagnetic CSS

Figures 5(a) and 5(b) plot  $f$  versus  $H_{\text{res}}$  at  $T = 300$  and  $80$  K, in which  $\theta$  was fixed at  $45^\circ$ . The experimental results obey Kittel's equation of  $f = (\gamma/2\pi)\sqrt{(H_{\text{res}} + H_{\text{ani}})(H_{\text{res}} + 4\pi M_{\text{eff}})}$ , where  $H_{\text{ani}}$  is the anisotropy field in the film plane and  $4\pi M_{\text{eff}}$  is the effective demagnetizing field. The numerical fits using the above Kittel relation give the values of  $H_{\text{ani}}$  and  $M_{\text{eff}}$ :  $H_{\text{ani}} = 21$  Oe and  $M_{\text{eff}} = 689$  emu  $\text{cm}^{-3}$  for  $T = 300$  K; and  $H_{\text{ani}} = 35$  Oe and  $M_{\text{eff}} = 692$  emu  $\text{cm}^{-3}$  for  $T = 80$  K. These values mean that there is no remarkable temperature

dependence in the magnetic properties. As shown in Fig. 5(c) representing the  $M$ - $T$  curve for the 2-nm-thick CFB film, the value of  $M$  for the CFB layer keeps almost constant in the temperature range below  $300$  K. Thus, the ST-FMR signal at  $T = 80$  K comes from the magnetic resonance of CFB magnetization as well as the result at  $T = 300$  K. All the ST-FMR signals in the present experiment are attributable to the CFB magnetization dynamics and are not contaminated with the CSS magnetization even at  $T$  lower than  $T_C$ .

Figure 5(d) plots the  $f$  dependence of  $V_S/V_A$  obtained from the spectra measured at  $T = 80$  K and  $\theta = 45^\circ$ .  $V_{\text{dc}}$  sometimes involves the contribution of spin pumping from FM and subsequent inverse SHE in NM [49], and the spin current generated by the spin pump is increased as  $f$  is increased [50]. One may be aware that  $V_S/V_A$  with the negative sign increases slightly with  $f$ , implying the small contribution of spin pump from CFB and inverse SHE in CSS. As shown in the next paragraph, however, the spin-pumping contribution is not so significant and does not affect the evaluation of spin-charge conversion efficiency.

Figure 5(e) summarizes the  $T$  dependence of  $V_S/V_A$  measured at  $f = 16$  GHz. The orange (green) marks represent the data obtained from the ST-FMR signal originating from AMR (GMR). At  $T \leq 150$  K, the ST-FMR signal originating from GMR appears. Near  $T_C$ , i.e., at  $T = 150$  K, the GMR contribution to the ST-FMR signal is quite small, giving rise to the remarkable error. With reducing  $T$  below  $100$  K, the sufficient GMR signal allows the accurate evaluation with the small error, which gives the values being consistent with the values from the ST-FMR signal originating from AMR. On the contrary,  $V_S/V_A$  from AMR at  $T = 50$  K exhibits the

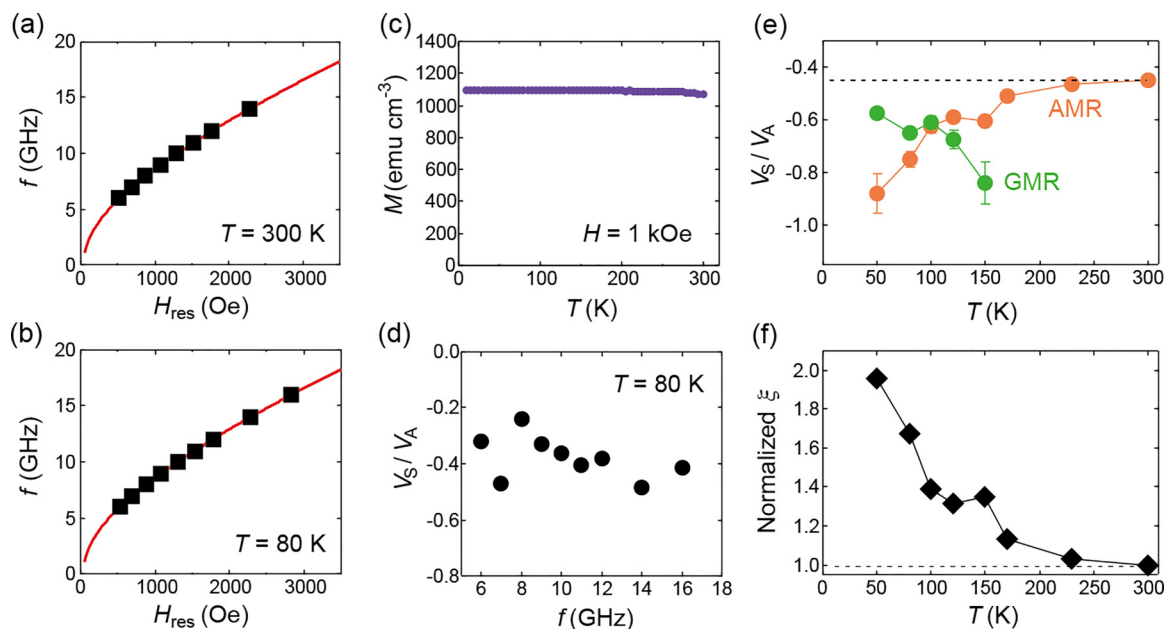


FIG. 5. (a) Resonant magnetic field ( $H_{\text{res}}$ ) vs  $f$  at  $T = 300$  K and (b)  $80$  K, where  $\theta$  was fixed at  $45^\circ$ . Solid squares denote the experimental data whereas the solid lines denote the results of fitting. (c)  $T$  dependence of magnetization ( $M$ ) for the 2-nm-thick CFB film measured at  $H = 1$  kOe. (d)  $f$  dependence of  $V_S/V_A$ , where  $\theta = 45^\circ$  and  $T = 80$  K. (e)  $T$  dependence of  $V_S/V_A$  obtained from the AMR (orange marks) and the GMR signals (green marks) measured at  $f = 16$  GHz. (f)  $T$  dependence of spin-charge conversion efficiency ( $\xi$ ) normalized by the value at  $T = 300$  K.

large error, which might be due to the small contribution of AMR to the ST-FMR signal compared to that of GMR at the low temperature. There are two important findings. First, the value of  $V_S/V_A$  is definitely increased at  $T \leq T_C$ , suggesting that the phase transition to the ferromagnetic CSS leads to the enhancement of spin-charge conversion efficiency. Second, the small GMR signal at  $T \sim T_C$  gives rise to the large error, resulting in the overestimation of  $V_S/V_A$ , and the results from the sufficient AMR signal suggest no particular jump in  $V_S/V_A$  at  $T \sim T_C$  in the case of CSS. Here, let us discuss again the contribution of spin pumping and subsequent inverse SHE. The field angular dependence of spin-pump contribution is the same as that for SHT detected through the AMR. However, the field angular dependence of SHT detected by GMR is totally different from that of spin-pumping process. Since the value of  $V_S/V_A$  from AMR is fairly in agreement with that from GMR at  $80 \leq T \leq 120$  K, we consider that the spin-pumping contribution is not so significant.

Then, the spin-charge conversion efficiency ( $\xi$ ) via SHE and/or SAHE is calculated. In order to take into account the contribution of SAHE as well as SHE,  $\alpha_{SH}$  in Eq. (3) is replaced with  $\xi$ , and the relationship between  $\xi$  and  $V_S/V_A$  is given by

$$\xi = -\frac{V_S}{V_A} \frac{e\mu_0 M_s^{\text{CFB}} d^{\text{CFB}} d^{\text{CSS}} \eta^{\text{CSS+Cu}}}{\hbar \eta^{\text{CSS}}} \sqrt{\frac{H + 4\pi M_{\text{eff}}}{H + H_{\text{ani}}}}. \quad (7)$$

As discussed in Figs. 5(a)–5(c), the magnetic properties for CFB do not show the remarkable temperature dependence. In addition, we assume that  $\eta^{\text{CSS+Cu}}/\eta^{\text{CSS}}$  is almost constant against  $T$  because of the small monotonic change in  $R_{xx}$  for the CSS/Cu/CFB trilayer [Fig. 2(g)]. Then, we simply consider that  $\xi$  is proportional to  $V_S/V_A$ . Figure 5(f) plots the  $T$  dependence of  $\xi$  normalized by the value of  $\xi$  at  $T = 300$  K, where the values of  $V_S/V_A$  from the AMR were used. It is noted that  $\xi$  at  $T = 50$  K is nearly twice as large than that at  $T = 300$  K. In our previous work [42], we carefully evaluated  $\xi$  to be 0.10 at room temperature employing the similar ST-FMR method. By using this room-temperature value, we obtain  $\xi = 0.20$  at  $T = 50$  K. This  $\xi$  may be an overestimated value because  $V_S/V_A$  from the AMR at  $T = 50$  K exhibits the larger error in Fig. 5(e). However, we can conclude that  $\xi$  becomes more than 0.13 at  $T \leq 150$  K taking into account the  $V_S/V_A$  evaluated not only from the AMR but also from the GMR.

### E. Discussion

In this subsection, first, we again emphasize the importance of taking into account the signal through the GMR effect for analyzing the angular dependence of ST-FMR spectra. Sometimes, ST-FMR studies for trilayered structures consisting of FM/NM/FM might overlook the contribution of GMR effect. If the trilayer exhibits a non-negligible GMR effect, one needs to take into account the contribution of ST-FMR signal through the GMR as demonstrated in Figs. 4(c) and 4(d). Otherwise, the angular dependence of ST-FMR signal cannot be analyzed correctly. Although we cannot separate the contribution of SAHE from the SHT by the present

numerical fitting, the following argument helps us to reveal the contribution of SAHE. In Table I, one can see that the signs of  $V_S^{\text{Oe,oopGMR}}$  are negative and positive for +5-kOe field cooling and –5-kOe field cooling, respectively. This means that the magnetization directions of out-of-plane hard magnetic CSS are opposite between two field-cooling conditions, although we are not sure how the in-plane  $H$  affected the out-of-plane magnetization at present. An important point is that the sign of SPT depends on the sign of out-of-plane magnetization, while the sign of SAHE does not change regardless of the sign of magnetization direction. Since both SPT due to the out-of-plane hard magnetic CSS and SAHE in the in-plane hard magnetic CSS involve the  $\sin\theta$  term, there is possibility that the compensation of SPT and SAHE gives rise to the small  $V_S^{\text{SPT,GMR}}$  and  $V_S^{\text{SPT,AMR}}$ . However, the contribution of SPT is reversed when out-of-plane hard magnetic CSS magnetization is reversed whereas the contribution of SAHE is not reversed, and the small  $V_S^{\text{SPT,GMR}}$  and  $V_S^{\text{SPT,AMR}}$  are experimentally obtained for both out-of-plane magnetization directions. These facts indicate that the compensation cannot explain the small  $V_S^{\text{SPT,GMR}}$  and  $V_S^{\text{SPT,AMR}}$ , and we can conclude the negligible contribution of SPT. At the same time, we may say that the SAHE in the in-plane CSS is also negligibly small. In Appendix E, we also discuss other possible torques, which are not taken into account in the above discussion.

Next, the magnitude and the mechanism of spin-charge conversion are discussed. The present CSS shows  $\xi$  more than 0.13 at  $T \leq 150$  K. This  $\xi$  is much higher than that for another magnetic Weyl semimetal  $\text{Co}_2\text{MnGa}$  showing  $\xi = -0.078$  [25]. Then, we conclude that the ferromagnetic CSS is a material showing highly efficient spin-charge conversion. When the ST-FMR spectra are analyzed in this study, the three regions, i.e., in-plane soft magnetic CSS, in-plane hard magnetic CSS, and out-of-plane hard magnetic CSS, are regarded as a single source for generating  $J_s$  and those contributions are not separated. Among them, we examine the  $J_s$  generation through the SHE in the out-of-plane hard magnetic CSS with the help from the theoretical calculation, which is given in the next section.

## IV. THEORETICAL CALCULATION

### A. Effective tight-binding model of CSS

In this section, we introduce an effective tight-binding model of CSS [51] to theoretically study the intrinsic SHE from CSS. This model reproduces the Weyl points and the nodal-line configurations in momentum space, which are similar to those obtained by *ab initio* calculations [30,52,53]. In this model, we consider one of  $d$  orbitals from Co and  $p_z$  orbital from the interkagome-layer Sn, which are anticipated to be located near the Fermi level ( $E_F$ ). For simplicity, all other orbitals are neglected. We set primitive translation vectors as  $\mathbf{a}_1 = (\frac{a}{2}, 0, c)$ ,  $\mathbf{a}_2 = (-\frac{a}{4}, \frac{\sqrt{3}a}{4}, c)$ , and  $\mathbf{a}_3 = (-\frac{a}{4}, -\frac{\sqrt{3}a}{4}, c)$ . In the following we set  $c = \frac{\sqrt{3}a}{2}$ . The total Hamiltonian is given by

$$H = H_{d-p} + H_{\text{so}} + H_{\text{exc}}. \quad (8)$$

Here,  $H_{d-p}$  is the spin-independent hopping term,

$$H_{d-p} = - \sum_{ij\sigma} [t_{ij} d_{i\sigma}^\dagger d_{j\sigma} + t_{ij}^{dp} (d_{i\sigma}^\dagger p_{j\sigma} + p_{i\sigma}^\dagger d_{j\sigma}) + \epsilon_p p_{i\sigma}^\dagger p_{i\sigma}]. \quad (9)$$

$d_{j\sigma}$  and  $p_{i\sigma}$  are the annihilation operators of  $d$  orbital on Co and  $p$  orbital on Sn, respectively.  $t_{ij}$  includes the nearest- and second-nearest neighbor hopping,  $t_1$  and  $t_2$  in the intrakagome layer, and the interkagome layer  $t_z$ .  $t_{ij}^{dp}$  is the hybridization between the  $d$  orbital and  $p$  orbital.  $\epsilon_p$  is the on-site potential of the  $p$  orbital on Sn.

$H_{so}$  is a spin-orbit coupling (SOC) term given by  $H_{so} = H_{so}^{KM} + H_{so}^z$ . Here,  $H_{so}^{KM}$  and  $H_{so}^z$  are intrakagome-layer Kane-Male (KM)-type SOC [54] and interlayer-kagome SOC [55], respectively, given as

$$H_{so}^{KM} = -it_{so}^{KM} \sum_{\langle\langle ij \rangle\rangle\sigma\sigma'} v_{ij} d_{i\sigma}^\dagger \sigma_{\sigma\sigma'}^z d_{j\sigma'}, \quad (10)$$

and

$$H_{so}^z = -it_{so}^z \sum_{\langle\langle ij \rangle\rangle\sigma\sigma'} \eta_{ij} \cdot d_{i\sigma}^\dagger \sigma_{\sigma\sigma'} d_{j\sigma'}. \quad (11)$$

In Eq. (10),  $t_{so}^{KM}$  is the hopping strength and the summation  $ij$  is about intrakagome-layer second-nearest neighbor sites.  $v_{ij} = +1(-1)$ , when the electron hops counterclockwise (clockwise) to get to the next-nearest neighbor site on kagome plane. In Eq. (11),  $t_{so}^z$  is the hopping strength and the summation is about interkagome-layer nearest-neighbor hopping. Here,  $\eta_{ij}$  is given by  $\eta_{CA} = \frac{a_1}{2} \times \frac{a_3}{2} / |\frac{a_1}{2} \times \frac{a_3}{2}|$ ,  $\eta_{AB} = \frac{a_2}{2} \times \frac{a_1}{2} / |\frac{a_2}{2} \times \frac{a_1}{2}|$ , and  $\eta_{BC} = \frac{a_3}{2} \times \frac{a_2}{2} / |\frac{a_3}{2} \times \frac{a_2}{2}|$ . Interkagome-layer SOC [Eq. (11)] plays an important role to obtain the finite SHC  $\sigma_{xz}^{sy}$ .

$H_{exc}$  is the exchange-coupling term between spins of itinerant electrons and magnetization, which is given by

$$H_{exc} = -J \sum_{i\sigma\sigma'} \mathbf{m} \cdot (d_{i\sigma}^\dagger \sigma_{\sigma\sigma'} d_{i\sigma'} + p_{i\sigma}^\dagger \sigma_{\sigma\sigma'} p_{i\sigma'}). \quad (12)$$

Here,  $J$  is the exchange coupling constant and  $\mathbf{m}$  is the dimensionless magnetization vector. We here consider the exchange coupling on the Sn site for simplicity. In the following, we set  $t_1$  as a unit of energy,  $t_2 = 0.6t_1$ ,  $t^{dp} = 1.8t_1$ ,  $t_z = -1.0t_1$ ,  $\epsilon_p = -7.2t_1$ ,  $t_{so}^{KM} = -0.2t_1$ , and  $J = 1.2t_1$ . These parameters were chosen so that the configurations of the nodal rings are similar to those obtained by *ab initio* calculations [52,53]. The chemical potential  $\mu$  is determined by using the formula

$$n_e = \int_{-\infty}^{\infty} d\epsilon \rho(\epsilon) f_{FD}(\epsilon - \mu, T). \quad (13)$$

Here,  $n_e$  is the number of the electrons per unit cell and being set as  $n_e = 3$  in our CSS model, as discussed in Refs. [51,55].  $\rho(\epsilon)$  is the density of states as a function of the energy and  $f_{FD}$  is the Fermi-Dirac distribution function. In the following subsection, the intrinsic SHE is studied based on the effective tight-binding model.

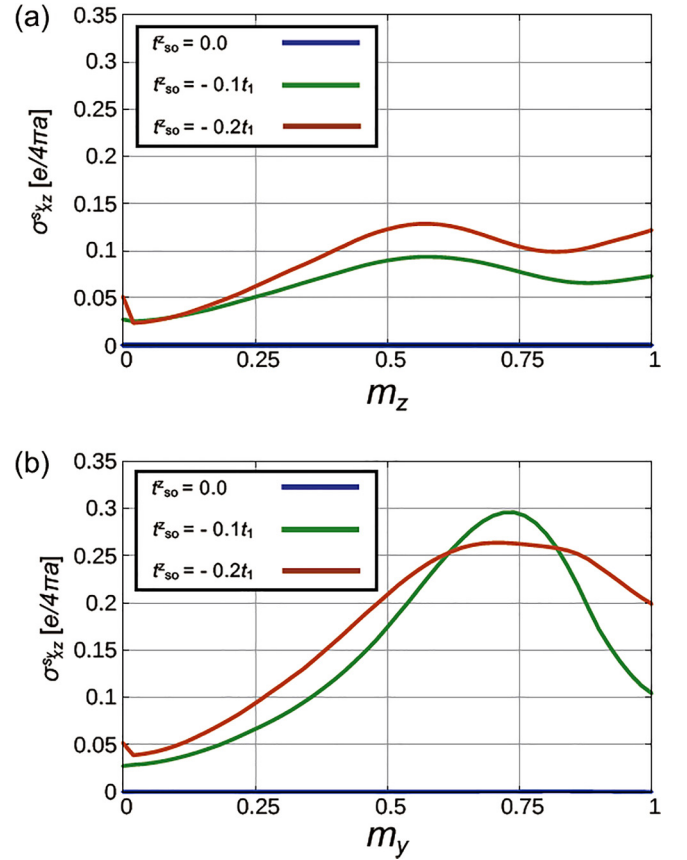


FIG. 6. Magnetic-moment amplitude dependence of the spin Hall conductivities for the CSS model with (a) out-of-plane magnetization and (b) in-plane magnetization for  $t_{so}^z = 0.0, -0.1t_1$  and  $t_{so}^z = -0.2t_1$ .

## B. Enhancement of spin Hall conductivity

Then, we study the intrinsic SHE with FM ordering by the CSS model. An enhancement of the spin Hall conductivity (SHC) is found in both out-of-plane and in-plane cases as shown in Fig. 6. We focus on the SHC when the electric field is applied to the  $x$  direction and the spin current with  $s_y$  flows to the  $z$  direction (out-of-plane direction). The SHC characterizing this situation  $\sigma_{xz}^{sy}$  is obtained by the Kubo formula [2],

$$\sigma_{xz}^{sy} = \frac{e}{4\pi a} \sum_{n \neq m \text{ BZ}} \int i \frac{d^3k}{(2\pi)^2} \frac{(f_{FD}(E_{nk}) - f_{FD}(E_{mk}))}{E_{mk} - E_{nk}} \times \frac{\langle nk | v_x | mk \rangle \langle mk | j_z^{sy} | nk \rangle}{(E_{mk} - E_{nk} + i\eta)}. \quad (14)$$

Here,  $v_i$  ( $i = x, y$ ) is the velocity operator given by  $v_i = \frac{1}{\hbar} \frac{\partial H(\mathbf{k})}{\partial k_i}$ . The spin-current operator is given by  $j_z^{sy} = \frac{\hbar}{2} \{v_z, \sigma_y\}$  (Ref. [2]), where  $\sigma_y$  is the  $y$  component of vector of Pauli matrices. The eigenstates  $|n\mathbf{k}\rangle$  are obtained by diagonalizing the total Hamiltonian [Eq. (8)]. Figure 6 shows the SHC as a function of the amplitude of the magnetic moment using different FM orderings: Fig. 6(a) out-of-plane FM ordering  $\mathbf{m} = (0, 0, m_z)$  and Fig. 6(b) in-plane magnetic ordering  $\mathbf{m} = (0, m_y, 0)$ . The system is paramagnetic when  $m_z = 0$ , whereas the system is fully polarized when  $m_z = 1.0$ . The SHC is

calculated with different strengths of the interlayer SOC, for  $t_{\text{so}}^z = 0.0, -0.1t_1$ , and  $-0.2t_1$ . In both cases of out-of-plane and in-plane magnetic orders, it is apparent that the SHC enhances as  $m$  increases. These results are consistent with the enhancement of the spin-charge efficiency experimentally observed at  $T < T_C$ .

## V. CONCLUSION

The characteristic  $T$  dependence of spin-charge conversion for the CSS was found by measuring the ST-FMR for the trilayer consisting of CSS/Cu/CFB. Below  $T = 150$  K, where the present CSS layer exhibited the ferromagnetic phase, not only the AMR but also the GMR contributed to the ST-FMR signal. By taking into account the  $V_{\text{dc}}$  originating from GMR, we successfully explained the field angular dependence of  $V_{\text{dc}}$  observed at  $T < T_C$ . We revealed that the SHT involving the torques coming from SHE and/or SAHE plays the major role in the spin torque acting on CFB and the contribution of spin precession process to the spin-torque is negligibly small. A definite increase in  $\xi$  was observed at  $T < T_C$ , indicating that the phase transition to the ferromagnetic CSS leads to the enhancement of spin-charge conversion efficiency. The experimental tendency was supported by the theoretical calculation, which showed the increase in spin Hall conductivity with the emergence of magnetic moment at  $T < T_C$ .

## ACKNOWLEDGMENTS

The authors are grateful to K. Takanashi for valuable discussion and T. Sasaki for her help in the film preparation using the ion beam sputtering. This work was supported by JSPS KAKENHI Grant-in-Aid for Scientific Research (A) (Grant No. JP20H00299), Grant-in-Aid for Early-Career Scientists (Grant No. JP20K15156), Grant-in-Aid for Scientific Research (B) (Grant No. JP20H01830), GP-Spin at Tohoku University, and JST CREST (Grant No. JPMJCR18T2).

## APPENDIX A: $R_{xy}$ VERSUS $H$ FOR CSS SINGLE-LAYER SAMPLE

Figure 7 shows the  $R_{xy}$  as functions of out-of-plane  $H$  and in-plane  $H$  for the CSS-single-layer sample without CFB, where the thickness of CSS is 9 nm and  $T$  was set at 100 K. The CSS single-layer sample was prepared using the identical blanket film for the CSS/Cu/CFB, but after the etching process, the CSS layer was capped by the Al-O layer.  $R_{xy}$  under the perpendicular  $H$  (black curve) corresponds to a single-phase AHE hysteresis loop.  $R_{xy}$  under the in-plane  $H$  (red curve) shows only a small parabolic change even when large  $H = 70$  kOe is applied. These results suggest that very large in-plane  $H$  is needed to saturate the out-of-plane magnetized hard magnetic CSS along the in-plane direction. Also, the amount of in-plane magnetized CSS phase is too small to be observed in the AHE curve, in which the out-of-plane magnetized hard magnetic CSS is dominant. Considering the result of GMR shown in the main text, the in-plane magnetized hard and soft magnetic CSS phases are formed mainly at the interface with the Cu layer because the GMR is very sensitive to the interface condition.

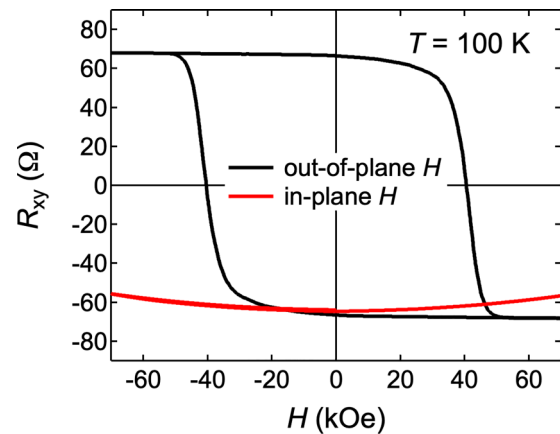


FIG. 7.  $R_{xy}$  as functions of out-of-plane  $H$  (black curve) and in-plane  $H$  (red curve) for the CSS single-layer sample without CFB, where the thickness of CSS is 9 nm and  $T$  was set at 100 K. For the  $R_{xy}$  vs in-plane  $H$  measurement, the CSS layer was magnetized in the  $-z$  direction at  $H = 0$  Oe due to the application of negative perpendicular  $H$  before the  $R_{xy}$  vs in-plane  $H$  measurement.

## APPENDIX B: TEMPERATURE DEPENDENCE OF MR CURVES FOR COPLANAR WAVEGUIDE DEVICE

In addition to the resistance of Hall device, the longitudinal resistance ( $R$ ) of the coplanar waveguide device for the ST-FMR measurement was measured by the two-probe method. Figure 8 shows MR curves for the coplanar waveguide device measured at (a)  $T = 300$  K, (b) 140 K, and (c) 50 K. At  $T = 300$  K, a small change in  $R$  is observed at low  $H$ , which is attributable to the AMR of CFB layer. As  $T$  is reduced to 140 K, the large  $R$  change appears, and the exchange-biased-like behavior is clearly observed in the MR curve measured at  $T = 50$  K.  $T$  dependence of  $R$  at  $H = 5$  kOe ( $R^{5\text{kOe}}$ ) and the resistance change ( $\Delta R^{\text{MAX}}$ ) is plotted in Fig. 8(d). One sees

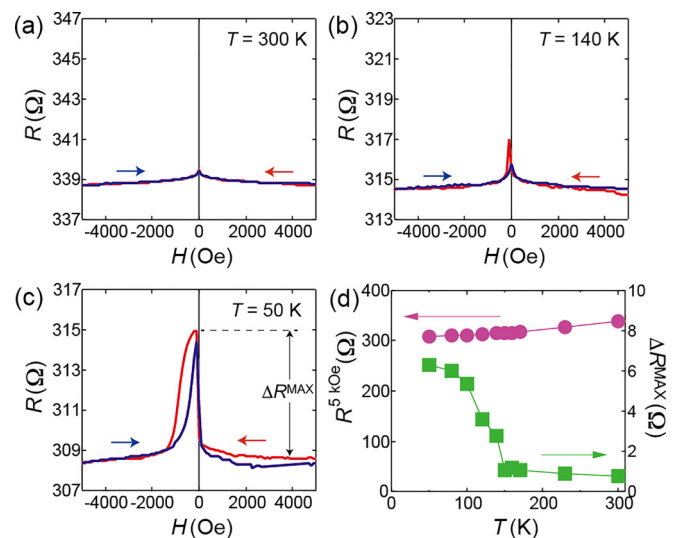


FIG. 8. MR curves for the coplanar waveguide device measured at (a)  $T = 300$  K, (b) 140 K, and (c) 50 K. Resistance for the coplanar waveguide device ( $R$ ) was measured using the two-probe method, and the in-plane  $H$  was applied at  $\theta = 45^\circ$ . (d)  $R$  at  $H = 5$  kOe ( $R^{5\text{kOe}}$ ) and the resistance change ( $\Delta R^{\text{MAX}}$ ), which is defined in (c), as a function of  $T$ .

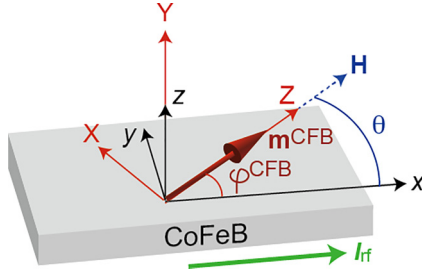


FIG. 9. Schematic illustration of two coordinate systems:  $(x, y, z)$  and  $(X, Y, Z)$ . In the equilibrium condition, the magnetic moment of CFB ( $\mathbf{m}^{\text{CFB}}$ ) is parallel to  $\mathbf{e}_z$ , which is also parallel to  $\mathbf{H}$ , i.e.,  $\varphi^{\text{CFB}} = \theta$ .  $I_{\text{rf}}$  was applied along  $\mathbf{e}_x$ .

that the coplanar waveguide devices exhibited the  $T$  dependence of device resistance similar to those observed for the Hall devices.

### APPENDIX C: DERIVATION OF EQUATIONS FOR RECTIFICATION dc VOLTAGE

Let us derive the  $V_{\text{dc}}$  through the AMR effect of CFB layer and the GMR effect coming from the relative magnetization angle between CFB and CSS layers. As mentioned in the main text, the in-plane angle of magnetic moment of CFB is defined as  $\varphi^{\text{CFB}}$ , and it is assumed that  $\mathbf{M}^{\text{CFB}}$  follows  $\mathbf{H}$  and, i.e.,  $\varphi^{\text{CFB}} = \theta$ .

In the coordinate depicted in Fig. 9, the device resistance ( $R$ ) taking into account the AMR, which depends on the unit vector of CFB magnetization ( $\mathbf{m}^{\text{CFB}}$ ), is given by

$$R(\mathbf{m}^{\text{CFB}}) = R_0 + \Delta R_{\text{AMR}} m_x^2, \quad (\text{C1})$$

where  $\mathbf{m}^{\text{CFB}} = m_x \mathbf{e}_x + m_y \mathbf{e}_y + m_z \mathbf{e}_z = m_x \mathbf{e}_x + m_y \mathbf{e}_y + m_z \mathbf{e}_z$ .  $m_y \mathbf{e}_y = m_z \mathbf{e}_z$ , then  $m_x \mathbf{e}_x + \mathbf{e}_z = m_x \mathbf{e}_x + m_y \mathbf{e}_y$ . Since  $m_x = \cos \theta - m_x \sin \theta$ , taking into account the first-order term,

$$R(\mathbf{m}^{\text{CFB}}) = R_0 + \Delta R_{\text{AMR}} \cos^2 \theta - \Delta R_{\text{AMR}} m_x \sin 2\theta + \dots \quad (\text{C2})$$

Next, we consider the device resistance change through the GMR effect. The experimental MR curves suggest that the GMR comes from the relative angle of magnetization between the CFB and the in-plane magnetized hard magnetic CSS ( $\mathbf{m}^{\text{CSS,hard}}$ ). Then,  $R(\mathbf{m}^{\text{CFB}})$  is given by

$$R(\mathbf{m}^{\text{CFB}}) = R_0 - \frac{\Delta R_{\text{GMR}}}{2} (\mathbf{m}^{\text{CFB}} \cdot \mathbf{m}^{\text{CSS,hard}}), \quad (\text{C3})$$

where  $\mathbf{m}^{\text{CSS,hard}} = m'_x \mathbf{e}_x + m'_z \mathbf{e}_z$ . The in-plane angle of magnetization of hard magnetic CSS is defined as  $\varphi^{\text{CSS,hard}}$ ; then,  $\mathbf{m}^{\text{CFB}} \cdot \mathbf{m}^{\text{CSS,hard}} = m_x m'_x + m'_z = m_x \sin(\theta - \varphi^{\text{CSS,hard}}) + \cos(\theta - \varphi^{\text{CSS,hard}})$ . Equation (C3) can be rewritten into

$$R(\mathbf{m}^{\text{CFB}}) = R_0 - \frac{\Delta R_{\text{GMR}}}{2} [m_x \sin(\theta - \varphi^{\text{CSS,hard}}) + \cos(\theta - \varphi^{\text{CSS,hard}})]. \quad (\text{C4})$$

Next, we consider the magnetization dynamics under the effective magnetic field ( $\mathbf{H}_{\text{eff}}$ ) and the external torque ( $\boldsymbol{\tau}$ ) is

given by the following Landau-Lifshitz-Gilbert equation:

$$\frac{d\mathbf{m}^{\text{CFB}}}{dt} = -\gamma \mu_0 \mathbf{m}^{\text{CFB}} \times \mathbf{H}_{\text{eff}} + \alpha \mathbf{m}^{\text{CFB}} \times \frac{d\mathbf{m}^{\text{CFB}}}{dt} + \boldsymbol{\tau}, \quad (\text{C5})$$

where  $\boldsymbol{\tau}$  includes spin-transfer torque and current-induced Oersted field torque, which comes from the rf current with the angular frequency of  $\omega_p$ .  $\boldsymbol{\tau}$  is expressed as

$$\tau_x(t) = \tau_x^0 \cos(\omega_p t), \quad (\text{C6})$$

$$\tau_y(t) = \tau_y^0 \cos(\omega_p t). \quad (\text{C7})$$

By linearizing Eq. (C5), small deviations of magnetization from the equilibrium points along the  $X$  and  $Y$  directions are expressed as

$$m_x(t) = C_X \cos(\omega_p t) + D_X \sin(\omega_p t), \quad (\text{C8})$$

$$m_y(t) = C_Y \cos(\omega_p t) + D_Y \sin(\omega_p t). \quad (\text{C9})$$

In Eqs. (C8) and (C9), phase components same as those of rf current torque of Eqs. (C6) and (C7) are detected as a rectification voltage.  $C_X$  and  $C_Y$  are

$$C_X = \frac{1}{\delta} L_S(\omega_p) \tau_x^0 + \frac{1}{\delta} \sqrt{\frac{H_{YY}}{H_{XX}}} L_A(\omega_p) \tau_y^0, \quad (\text{C10})$$

$$C_Y = -\frac{1}{\delta} \sqrt{\frac{H_{YY}}{H_{XX}}} L_A(\omega_p) \tau_x^0 + \frac{1}{\delta} L_S(\omega_p) \tau_y^0, \quad (\text{C11})$$

where  $L_{S(A)}$  represents the symmetric (antisymmetric) Lorentzian function and  $\delta$  is the resonance linewidth.  $L_S(\omega_p)$  and  $L_A(\omega_p)$  are given by

$$L_S(\omega_p) = \frac{(\delta/2)^2}{(\omega_p - \omega_0)^2 + (\delta/2)^2} \quad (\text{C12})$$

$$L_A(\omega_p) = \frac{(\omega_p - \omega_0)(\delta/2)}{(\omega_p - \omega_0)^2 + (\delta/2)^2}. \quad (\text{C13})$$

Using the relationship of  $\delta = (d\omega_0/dH)\Delta H$ , Eqs. (C12) and (C13) are transformed into

$$L_S(H) = \frac{(\Delta H/2)^2}{(H_{\text{res}} - H)^2 + (\Delta H/2)^2}, \quad (\text{C14})$$

$$L_A(H) = \frac{(H_{\text{res}} - H)(\Delta H/2)}{(H_{\text{res}} - H)^2 + (\Delta H/2)^2}, \quad (\text{C15})$$

where  $H_{\text{res}}$  represents the resonance magnetic field.

Here, ‘‘torque originating from SHE ( $\tau_{\text{SHE}}$ ),’’ ‘‘torque originating from spin precession ( $\tau_{\text{SP}}$ )’’ for  $\tau_x^0$ , and ‘‘current-induced Oersted field torque ( $\tau_{\text{Oe}}$ )’’ for  $\tau_y^0$  are considered. The quantization axis of spin generated by the SHE of CSS is along  $\mathbf{e}_y = \sin \theta \mathbf{e}_z + \cos \theta \mathbf{e}_x$ . This means that  $\tau_{\text{SHE}}$  shows the angular dependence of  $\cos \theta$  as shown in Eq. (3). On the other hand, the quantization axis of spin generated by the spin precession by the out-of-plane magnetized CSS ( $\mathbf{m}^{\text{CSS,OOP}}$ ) is along  $\mathbf{m}^{\text{CSS,OOP}} \times (\mathbf{e}_z \times \mathbf{E})$ , where  $\mathbf{E}$  is the applied electric field. Since  $\mathbf{m}^{\text{CSS,OOP}} = \mathbf{e}_z$  and  $\mathbf{E} = \mathbf{e}_x$ ,  $\mathbf{m}^{\text{CSS,OOP}} \times (\mathbf{e}_z \times \mathbf{E}) = \mathbf{e}_x = \cos \theta \mathbf{e}_z - \sin \theta \mathbf{e}_x$ . This means that  $\tau_{\text{SP}}$  shows the angular dependence of  $\sin \theta$ .

Then,  $\tau_{\text{SP}}$  is expressed as

$$\tau_{\text{SP}} = -\alpha_{\text{SP}} \frac{\gamma \hbar}{2eM_s d^{\text{CFB}} d^{\text{CSS}}} (I_{\text{rf}} \eta_{\text{CSS}}) \sin \theta, \quad (\text{C16})$$

where  $\alpha_{\text{SP}}$  represents the spin-charge conversion efficiency through the spin precession process. In addition to the SPT by  $\mathbf{m}^{\text{CSS, OOP}}$ , we may expect the SPT by in-plane magnetized  $\mathbf{m}^{\text{CSS, hard}}$ . That shows the symmetry of  $\mathbf{m}^{\text{CFB}} \times [(\mathbf{m}^{\text{CSS, hard}} \times \mathbf{e}_y) \times \mathbf{m}^{\text{CFB}}] = \cos \varphi^{\text{CSS, hard}} \mathbf{e}_y$ , which is defined as  $\tau_{\text{SP, ip}}$ .  $\tau_{\text{Oe}}$  is given by  $\tau_{\text{Oe}} = -\gamma \mu_0 \mathbf{m}^{\text{CFB}} \times \mathbf{H}_{\text{Oe}}$ , where  $\mathbf{H}_{\text{Oe}}$  is the Oersted field along  $-\mathbf{e}_y$  and given by  $\mathbf{H}_{\text{Oe}} = -(I_{\text{rf}} \eta_{\text{Cu+CSS}}/2w) \mathbf{e}_y$ . Then, we obtained Eq. (4). In summary, since  $\tau_X^0 = \tau_{\text{SHE}} + \tau_{\text{SP}}$  and  $\tau_Y^0 = \tau_{\text{Oe}} + \tau_{\text{SP, ip}}$ ,

$$\tau_X^0 = \frac{\gamma \hbar I_{\text{rf}} \eta_{\text{CSS}}}{2eM_s d^{\text{CFB}} d^{\text{CSS}}} (\alpha_{\text{SH}} \cos \theta - \alpha_{\text{SP}} \sin \theta), \quad (\text{C17})$$

$$\begin{aligned} \tau_Y^0 &= \mu_0 \frac{\gamma I_{\text{rf}} \eta_{\text{Cu+CSS}}}{2w} \cos \theta \\ &+ \frac{\gamma \hbar I_{\text{rf}} \eta_{\text{CSS}}}{2eM_s d^{\text{CFB}} d^{\text{CSS}}} \alpha_{\text{SP, ip}} \cos \varphi^{\text{CSS, hard}}. \end{aligned} \quad (\text{C18})$$

Finally,  $V_{\text{dc}}$  through AMR and GMR effect is obtained. From Eqs. (C2) and (C4), the resistance change depending on  $m_X$ ,  $m_Y$  [ $\Delta R(m_X, m_Y)$ ] is given by

$$\begin{aligned} \Delta R(m_X, m_Y) &= \Delta R_{\text{AMR}} m_X \sin 2\theta \\ &- \frac{\Delta R_{\text{GMR}}}{2} m_X \sin(\theta - \varphi^{\text{CSS, hard}}). \end{aligned} \quad (\text{C19})$$

Then, the multiplication of  $\Delta R(m_X, m_Y)$  and  $I_{\text{rf}}$  leads to the time-independent voltage, which is

$$\begin{aligned} V_{\text{dc}} &= \langle R(m_X, m_Y) I_{\text{rf}} \rangle \\ &= \frac{1}{2} \Delta R_{\text{AMR}} C_X I \sin 2\theta \\ &- \frac{1}{4} \Delta R_{\text{GMR}} C_X I \sin(\theta - \varphi^{\text{CSS, hard}}), \end{aligned} \quad (\text{C20})$$

where

$$\begin{aligned} C_X &= \frac{1}{\delta} L_S(\omega_p) \left[ \frac{\gamma \hbar I_{\text{rf}} \eta_{\text{CSS}}}{2eM_s d^{\text{CFB}} d^{\text{CSS}}} (\alpha_{\text{SH}} \cos \theta - \alpha_{\text{SP}} \sin \theta) \right] \\ &+ \frac{1}{\delta} \sqrt{\frac{H_{YY}}{H_{XX}}} L_A(\omega_p) \left[ \mu_0 \frac{\gamma I_{\text{rf}} \eta_{\text{Cu+CSS}}}{2w} \cos \theta \right]. \end{aligned} \quad (\text{C21})$$

In addition to the GMR effect between the CFB and the in-plane magnetized hard magnetic CSS, the GMR effect due to the out-of-plane magnetized hard magnetic CSS, which is called oop-GMR in this study, is needed to be taken into account when we discuss the rectification effect coming from the magnetization dynamics because the precession of  $\mathbf{m}^{\text{CFB}}$  possesses the out-of-plane component of magnetization. In this configuration,  $\mathbf{m}^{\text{CFB}} \cdot \mathbf{m}^{\text{CSS, OOP}} = m_Y$ , leading to  $R(\mathbf{m}^{\text{CFB}}) = R_0 - \frac{\Delta R_{\text{GMR}}}{2} m_Y$ . Then,  $\Delta R(\mathbf{m}^{\text{CFB}}) = \frac{\Delta R_{\text{GMR}}}{2} [\frac{1}{\delta} \sqrt{H_{YY}/H_{XX}} L_A(\omega_p) \tau_X^0 - \frac{1}{\delta} L_S(\omega_p) \tau_Y^0]$ . This gives rise to  $90^\circ$  phase shift of the ST-FMR spectral shape from the GMR case with in-plane CFB and in-plane CSS [Eqs. (C20) and (C21)]. Namely, the oop-GMR does not show the  $\theta$  dependence while it depends on the out-of-plane component of

$\mathbf{m}^{\text{CFB}}$ , which leads to only the phase shift in the effective torque direction by  $\pi/2$ .

#### APPENDIX D: SYMMETRIES OF $\tau_X^0$ ORIGINATING FROM SHE, SAHE, AND SPIN PRECESSION

In the case of  $\mathbf{E} // \mathbf{x}$ , the SHE of CSS generates  $J_s$  flowing along the  $z$  direction with the quantization axis of spin along  $\mathbf{e}_y$ . Thus, the  $\tau_X^0$  coming from the SHE has the symmetry of  $\mathbf{m}^{\text{CFB}} \times [(\mathbf{e}_z \times \mathbf{E}) \times \mathbf{m}^{\text{CFB}}]$ .

Next, let us consider the symmetry of SAHE related with the magnetic moment for in-plane hard magnetic CSS.  $J_s$  due to the SAHE is proportional to  $\mathbf{m}^{\text{CSS, hard}} \times \mathbf{E}$ . Then, the  $\tau_X^0$  coming from the SAHE has the symmetry of  $(\mathbf{m}^{\text{CSS, hard}} \times \mathbf{E}) \cdot \mathbf{e}_z [(\mathbf{m}^{\text{CFB}} \times \mathbf{m}^{\text{CSS, hard}}) \times \mathbf{m}^{\text{CFB}}]$ .

As described in Appendix C, the quantization axis of spin generated by the spin precession by the out-of-plane magnetized CSS is along  $\mathbf{m}^{\text{CSS, OOP}} \times (\mathbf{e}_z \times \mathbf{E}) = \mathbf{m}^{\text{CSS, OOP}} \times \mathbf{e}_y$ . Then, the  $\tau_X^0$  coming from the spin precession by the out-of-plane magnetized CSS has the symmetry of  $\mathbf{m}^{\text{CFB}} \times [(\mathbf{m}^{\text{CSS, OOP}} \times \mathbf{e}_y) \times \mathbf{m}^{\text{CFB}}]$ .

#### APPENDIX E: OTHER POSSIBLE TORQUES AND REMAINING EXPERIMENTS FOR MORE COMPREHENSIVE STUDY

The current analysis has taken into account all the possible dampinglike components of SHE, SAHE, and SPT. On the other hand, some fieldlike components are still neglected. For example, although the spin precession by the out-of-plane magnetized CSS leads to dampinglike torque with  $\mathbf{m}^{\text{CFB}} \times [(\mathbf{m}^{\text{CSS, OOP}} \times \mathbf{e}_y) \times \mathbf{m}^{\text{CFB}}]$ , simultaneously one may expect that the spin precession gives rise to the fieldlike torque with  $\mathbf{m}^{\text{CFB}} \times [(\mathbf{m}^{\text{CSS, OOP}} \times \mathbf{e}_y)]$ . This fieldlike torque is attributable to the imaginary part of spin-mixing conductance [9]. According to the previous paper of Ref. [9], the ratio between the real and imaginary parts of spin-mixing conductance roughly determines the ratio between the dampinglike and fieldlike components. Since some theoretical studies [56,57] reported that the imaginary part of spin-mixing conductance is one order of magnitude smaller than the real part, we expect that the contribution of fieldlike SPT is not significant. Thus, the current analysis does not contain the contribution of fieldlike SPT. However, such torques coming from the imaginary parts of spin-mixing conductance should be taken into account for a more comprehensive study.

In order to more clearly separate the contributions of torques, the following experiments will be useful: The ST-FMR measurement with different rf current directions allows us to distinguish the torques coming from the in-plane magnetized hard magnetic CSS. Also, it should be investigated how the application of out-of-plane magnetic field during the cooling affects the in-plane field angular dependence of ST-FMR. The out-of-plane magnetic field during the cooling will set the magnetization direction for the out-of-plane magnetized CSS. By changing the polarization of out-of-plane magnetized CSS, this ST-FMR measurement will give more information about the SPT. Those are remaining experiments for the comprehensive study.

- [1] A. Hoffman, Spin Hall effects in metals, *IEEE Trans. Magn.* **49**, 5172 (2013).
- [2] J. Sinova, S. O. Valenzuela, J. Wunderlich, C. H. Back, and T. Jungwirth, Spin hall effects, *Rev. Mod. Phys.* **87**, 1213 (2015).
- [3] B. F. Miao, S. Y. Huang, D. Qu, and C. L. Chien, Inverse Spin Hall Effect in a Ferromagnetic Metal, *Phys. Rev. Lett.* **111**, 066602 (2013).
- [4] S. M. Wu, J. Hoffman, J. E. Pearson, and A. Bhattacharya, Unambiguous separation of the inverse spin hall and anomalous nernst effects within a ferromagnetic metal using the spin seebeck effect, *Appl. Phys. Lett.* **105**, 092409 (2014).
- [5] T. Seki, K. Uchida, T. Kikkawa, Z. Qiu, E. Saitoh, and K. Takanashi, Observation of inverse spin Hall effect in ferromagnetic FePt alloys using spin Seebeck effect, *Appl. Phys. Lett.* **107**, 092401 (2015).
- [6] T. Taniguchi, J. Grollier, and M. D. Stiles, Spin-Transfer Torques Generated by the Anomalous Hall Effect and Anisotropic Magnetoresistance, *Phys. Rev. Appl.* **3**, 044001 (2015).
- [7] D. Tian, Y. Li, D. Qu, S. Y. Huang, X. Jin, and C. L. Chien, Manipulation of pure spin current in ferromagnetic metals independent of magnetization, *Phys. Rev. B* **94**, 020403(R) (2016).
- [8] V. P. Amin and M. D. Stiles, Spin transport at interfaces with spin-orbit coupling: Formalism, *Phys. Rev. B* **94**, 104419 (2016).
- [9] V. P. Amin and M. D. Stiles, Spin transport at interfaces with spin-orbit coupling: Phenomenology, *Phys. Rev. B* **94**, 104420 (2016).
- [10] C. Qin, S. Chen, Y. Cai, F. Kandaz, and Y. Ji, Nonlocal electrical detection of spin accumulation generated by anomalous Hall effect in mesoscopic  $\text{Ni}_{81}\text{Fe}_{19}$  films, *Phys. Rev. B* **96**, 134418 (2017).
- [11] K. S. Das, W. Y. Schoemaker, B. J. van Wees, and I. J. Vera-Marun, Spin injection and detection via the anomalous spin Hall effect of a ferromagnetic metal, *Phys. Rev. B* **96**, 220408(R) (2017).
- [12] S. Iihama, T. Taniguchi, K. Yakushiji, A. Fukushima, Y. Shiota, S. Tsunegi, R. Hiramatsu, S. Yuasa, Y. Suzuki, and H. Kubota, Spin-transfer torque induced by the spin anomalous Hall effect, *Nat. Electron.* **1**, 120 (2018).
- [13] J. D. Gibbons, D. MacNeill, R. A. Buhrman, and D. C. Ralph, Reorientable Spin Direction for Spin Current Produced by the Anomalous Hall Effect, *Phys. Rev. Appl.* **9**, 064033 (2018).
- [14] A. Bose, D. D. Lam, S. Bhuktare, S. Dutta, H. Singh, Y. Jibiki, M. Goto, S. Miwa, and A. A. Tulapurkar, Observation of Anomalous Spin Torque Generated by a Ferromagnet, *Phys. Rev. Appl.* **9**, 064026 (2018).
- [15] S. C. Baek, V. P. Amin, Y. W. Oh, G. Go, S. J. Lee, G. H. Lee, K. J. Kim, M. D. Stiles, B. G. Park, and K. J. Lee, Spin currents and spin-orbit torques in ferromagnetic trilayers, *Nat. Mater.* **17**, 509 (2018).
- [16] J. Cramer, A. Ross, S. Jaiswal, L. Baldrati, R. Lebrun, and M. Kläui, Orientation-dependent direct and inverse spin Hall effects in  $\text{Co}_{60}\text{Fe}_{20}\text{B}_{20}$ , *Phys. Rev. B* **99**, 104414 (2019).
- [17] T. Seki, S. Iihama, T. Taniguchi, and K. Takanashi, Large spin anomalous Hall effect in  $\text{Ll}_0\text{-FePt}$ : Symmetry and magnetization switching, *Phys. Rev. B* **100**, 144427 (2019).
- [18] Z. Wen, Z. Qiu, S. Tölle, C. Gorini, T. Seki, D. Hou, T. Kubota, U. Eckern, E. Saitoh, and K. Takanashi, Spin-charge conversion in  $\text{NiMnSb}$  Heusler alloy films, *Sci. Adv.* **5**, eaaw9337 (2019).
- [19] C. Safranski, E. A. Montoya, and I. N. Krivorotov, Spin-orbit torque driven by a planar Hall current, *Nat. Nanotechnol.* **14**, 27 (2019).
- [20] Y. Omori, E. Sagasta, Y. Niimi, M. Gradhand, L. E. Hueso, F. Casanova, and Y. C. Otani, Relation between spin Hall effect and anomalous Hall effect in 3d ferromagnetic metals, *Phys. Rev. B* **99**, 014403 (2019).
- [21] Y. Hibino, K. Hasegawa, T. Koyama, and D. Chiba, Spin-orbit torque generated by spin-orbit precession effect in  $\text{Py/Pt/Co}$  trilayer structure, *APL Mater.* **8**, 041110 (2020).
- [22] Y. Hibino, K. Yakushiji, A. Fukushima, H. Kubota, and S. Yuasa, Spin-orbit torque generated from perpendicularly magnetized  $\text{Co/Ni}$  multilayers, *Phys. Rev. B* **101**, 174441 (2020).
- [23] A. Yagmur, S. Sumi, H. Awano, and K. Tanabe, Large Inverse Spin Hall Effect in  $\text{Co-Tb}$  Alloys due to Spin Seebeck Effect, *Phys. Rev. Appl.* **14**, 064025 (2020).
- [24] Y. Koike, S. Iihama, and S. Mizukami, Composition dependence of the spin-anomalous Hall effect in a ferromagnetic  $\text{Fe-Co}$  alloy, *Jpn. J. Appl. Phys.* **59**, 090907 (2020).
- [25] K. Tang, Z. Wen, Y.-C. Lau, H. Sukegawa, T. Seki, and S. Mitani, Magnetization switching induced by spin-orbit torque from  $\text{Co}_2\text{MnGa}$  magnetic Weyl semimetal thin films, *Appl. Phys. Lett.* **118**, 062402 (2021).
- [26] L. Leiva, S. Granville, Y. Zhang, S. Dushenko, E. Shigematsu, T. Shinjo, R. Ohshima, Y. Ando, and M. Shiraishi, Giant spin Hall angle in the Heusler alloy Weyl ferromagnet  $\text{Co}_2\text{MnGa}$ , *Phys. Rev. B* **103**, L041114 (2021).
- [27] Y. Miura and K. Masuda, First-principles calculations on the spin anomalous Hall effect of ferromagnetic alloys, *Phys. Rev. Mater.* **5**, L101402 (2021).
- [28] A. R. Mellnik, J. S. Lee, A. Richardella, J. L. Grab, P. J. Mintun, M. H. Fischer, A. Vaezi, A. Manchon, E.-A. Kim, N. Samarth, and D. C. Ralph, Spin-transfer torque generated by a topological insulator, *Nature (London)* **511**, 449 (2014).
- [29] K. Kondou, R. Yoshimi, A. Tsukazaki, Y. Fukuma, J. Matsuno, K. S. Takahashi, M. Kawasaki, Y. Tokura, and Y. Otani, Fermi-level-dependent charge-to-spin current conversion by Dirac surface states of topological insulators, *Nat. Phys.* **12**, 1027 (2016).
- [30] E. Liu, Y. Sun, N. Kumar, L. Muechler, A. Sun, L. Jiao, S.-Y. Yang, D. Liu, A. Liang, Q. Xu, J. Kroder, V. Süß, H. Borrmann, C. Shekhar, Z. Wang, C. Xi, W. Wang, W. Schnelle, S. Wirth, Y. Chen, S. T. B. Goennenwein, and C. Felser, Giant anomalous Hall effect in a ferromagnetic Kagomé-lattice semimetal, *Nat. Phys.* **14**, 1125 (2018).
- [31] Q. Wang, Y. Xu, R. Lou, Z. Liu, M. Li, Y. Huang, D. Shen, H. Weng, S. Wang, and H. Lei, Large intrinsic anomalous Hall effect in half-metallic ferromagnet  $\text{Co}_3\text{Sn}_2\text{S}_2$  with magnetic Weyl fermions, *Nat. Commun.* **9**, 3681 (2018).
- [32] N. Morali, R. Batabyal, P. K. Nag, E. Liu, Q. Xu, Y. Sun, B. Yan, C. Felser, N. Avraham, and H. Beidenkopf, Fermi-arc diversity on surface terminations of the magnetic Weyl semimetal  $\text{Co}_3\text{Sn}_2\text{S}_2$ , *Science* **365**, 1286 (2019).
- [33] L. Jiao, Q. Xu, Y. Cheon, Y. Sun, C. Felser, E. Liu, and S. Wirth, Signatures for half-metallicity and nontrivial surface states in the kagome lattice Weyl semimetal  $\text{Co}_3\text{Sn}_2\text{S}_2$ , *Phys. Rev. B* **99**, 245158 (2019).
- [34] K. Fujiwara, J. Ikeda, J. Shiogai, T. Seki, K. Takanashi, and A. Tsukazaki, Ferromagnetic  $\text{Co}_3\text{Sn}_2\text{S}_2$  thin films fabricated by co-sputtering, *Jpn. J. Appl. Phys.* **58**, 050912 (2019).

- [35] J. Ikeda, K. Fujiwara, J. Shiogai, T. Seki, K. Nomura, K. Takanashi, and A. Tsukazaki, Critical thickness for the emergence of Weyl features in  $\text{Co}_3\text{Sn}_2\text{S}_2$  thin films, *Commun. Mater.* **2**, 18 (2021).
- [36] J. Ikeda, K. Fujiwara, J. Shiogai, T. Seki, K. Nomura, K. Takanashi, and A. Tsukazaki, Two-dimensionality of metallic surface conduction in  $\text{Co}_3\text{Sn}_2\text{S}_2$  thin films, *Commun. Phys.* **4**, 117 (2021).
- [37] I. Belopolski, T. A. Cochran, X. Liu, Z.-J. Cheng, X. P. Yang, Z. Guguchia, S. S. Tsirkin, J.-X. Yin, P. Vir, G. S. Thakur, S. S. Zhang, J. Zhang, K. Kaznatcheev, G. Cheng, G. Chang, D. Multer, N. Shumiya, M. Litskevich, E. Vescovo, T. K. Kim, C. Cacho, N. Yao, C. Felser, T. Neupert, and M. Z. Hasan, Signatures of Weyl Fermion Annihilation in a Correlated Kagome Magnet, *Phys. Rev. Lett.* **127**, 256403 (2021).
- [38] T. Kubodera, H. Okabe, Y. Kamihara, and M. Matoba, Ni substitution effect on magnetic and transport properties in metallic ferromagnet  $\text{Co}_3\text{Sn}_2\text{S}_2$ , *Physica B* **378-380**, 1142 (2006).
- [39] P. Vaqueiro and G. G. Sobany, A powder neutron diffraction study of the metallic ferromagnet  $\text{Co}_3\text{Sn}_2\text{S}_2$ , *Solid State Sci.* **11**, 513 (2009).
- [40] W. Schnelle, A. Leithe-Jasper, H. Rosner, F. M. Schappacher, R. Pöttgen, F. Pielhofer, and R. Wehrich, Ferromagnetic ordering and half-metallic state of  $\text{Sn}_2\text{Co}_3\text{S}_2$  with the shandite-type structure, *Phys. Rev. B* **88**, 144404 (2013).
- [41] M. A. Kassem, Y. Tabata, T. Waki, and H. Nakamura, Single crystal growth and characterization of kagomé-lattice shandites  $\text{Co}_3\text{Sn}_{2-x}\text{In}_x\text{S}_2$ , *J. Cryst. Growth* **426**, 208 (2015).
- [42] Y.-C. Lau, J. Ikeda, K. Fujiwara, A. Ozawa, T. Seki, K. Nomura, A. Tsukazaki, and K. Takanashi, Intercorrelated anomalous Hall and spin Hall effect in kagome-lattice  $\text{Co}_3\text{Sn}_2\text{S}_2$ -based shandite films, [arXiv:2203.02356](https://arxiv.org/abs/2203.02356).
- [43] D. H. Wei, Y. Niimi, B. Gu, T. Ziman, S. Maekawa, and Y. Otani, The spin Hall effect as a probe of nonlinear spin fluctuations, *Nat. Commun.* **3**, 1058 (2012).
- [44] Y. Ou, D. C. Ralph, and R. A. Buhrman, Strong Enhancement of the Spin Hall Effect by Spin Fluctuations near the Curie Point of  $\text{Fe}_x\text{Pt}_{1-x}$  Alloys, *Phys. Rev. Lett.* **120**, 097203 (2018).
- [45] L. Liu, T. Moriyama, D. C. Ralph, and R. A. Buhrman, Spin-Torque Ferromagnetic Resonance Induced by the Spin Hall Effect, *Phys. Rev. Lett.* **106**, 036601 (2011).
- [46] T. Seki, Y.-C. Lau, S. Iihama, and K. Takanashi, Spin-orbit torque in a Ni-Fe single layer, *Phys. Rev. B* **104**, 094430 (2021).
- [47] Z. Guguchia, J. A. T. Verezhak, D. J. Gawryluk, S. S. Tsirkin, J.-X. Yin, I. Belopolski, H. Zhou, G. Simutis, S.-S. Zhang, T. A. Cochran, G. Chang, E. Pomjakushina, L. Keller, Z. Skrzeczkowska, Q. Wang, H. C. Lei, R. Khasanov, A. Amato, S. Jia, T. Neupert, H. Luetkens, and M. Z. Hasan, Tunable anomalous Hall conductivity through volume-wise magnetic competition in a topological kagome magnet, *Nat. Commun.* **11**, 559 (2020).
- [48] E. Lachman, R. A. Murphy, N. Maksimovic, R. Kealhofer, S. Haley, R. D. McDonald, J. R. Long, and J. G. Analytis, Exchange-biased topological transverse thermoelectric effects in a Kagome ferrimagnet, *Nat. Commun.* **11**, 560 (2020).
- [49] O. Mosendz, J. E. Pearson, F. Y. Fradin, G. E. W. Bauer, S. D. Bader, and A. Hoffmann, Quantifying Spin Hall Angles from Spin Pumping: Experiments and Theory, *Phys. Rev. Lett.* **104**, 046601 (2010).
- [50] K. Ando, S. Takahashi, J. Ieda, Y. Kajiwara, H. Nakayama, T. Yoshino, K. Harii, Y. Fujikawa, M. Matsuo, S. Maekawa, and E. Saitoh, Inverse spin-Hall effect induced by spin pumping in metallic system, *J. Appl. Phys.* **109**, 103913 (2011).
- [51] A. Ozawa and K. Nomura, Two-orbital effective model for magnetic Weyl semimetal in kagome-lattice shandite, *J. Phys. Soc. Jpn.* **88**, 123703 (2019).
- [52] Q. Xu, E. Liu, W. Shi, L. Muechler, J. Gayles, C. Felser, and Y. Sun, Topological surface Fermi arcs in the magnetic Weyl semimetal  $\text{Co}_3\text{Sn}_2\text{S}_2$ , *Phys. Rev. B* **97**, 235416 (2018).
- [53] Y. Yanagi, J. Ikeda, K. Fujiwara, K. Nomura, A. Tsukazaki, and M.-T. Suzuki, First-principles investigation of magnetic and transport properties in hole-doped shandite compounds  $\text{Co}_3\text{Sn}_x\text{In}_{2-x}\text{S}_2$ , *Phys. Rev. B* **103**, 205112 (2021).
- [54] C. L. Kane and E. J. Mele, Quantum Spin Hall Effect in Graphene, *Phys. Rev. Lett.* **95**, 226801 (2005).
- [55] A. Ozawa and K. Nomura, Self-consistent analysis of doping effect for magnetic ordering in stacked-kagome Weyl system, *Phys. Rev. Mater.* **6**, 024202 (2022).
- [56] Q. Zhang, S. Hikino, and S. Yunoki, First-principles study of the spin-mixing conductance in Pt/Ni<sub>81</sub>Fe<sub>19</sub> junctions, *Appl. Phys. Lett.* **99**, 172105 (2011).
- [57] P. M. Haney, H.-W. Lee, K.-J. Lee, A. Manchon, and M. D. Stiles, Current induced torques and interfacial spin-orbit coupling: Semiclassical modeling, *Phys. Rev. B* **87**, 174411 (2013).